Integrating flexibility-based curvature with quasi-static features induced by traffic loads for high-resolution damage localization in bridges

Published in *Mechanical Systems and Signal Processing*
Volume 186, March 2023, Article 109907. https://doi.org/10.1016/j.ymssp.2022.109907

Integrating flexibility-based curvature with quasi-static features induced by traffic loads for high-resolution damage localization in bridges

Said Quqa[a,*] and Luca Landi[a]

[a] *Department DICAM, University of Bologna, Viale del Risorgimento 2, 40136 Bologna, Italy*

ABSTRACT

Curvature is one of the most popular damage-sensitive features in vibration-based structural health monitoring applications, typically calculated from identified modal features. While the relevant strategic or historical importance of bridges may justify dense sensor networks, a limited budget is generally assigned to monitor "minor" viaducts, thus involving inexpensive devices or extremely sparse sensing solutions. Modal parameters can only be obtained at instrumented locations. Thereby, damage assessment methods based on identified features typically have a low spatial resolution, especially when using low-cost monitoring setups with a modest number of sensing devices. This paper proposes an original identification method for the curvature of bridges based on sparse acceleration measurements that can be collected using standard accelerometers. The raw acceleration signal is processed through a particular filter bank that extracts dynamic and quasi-static signal components. The first components are employed to identify modal parameters, from which sparse yet robust estimates of the structural curvature are retrieved. On the other hand, the quasi-static acceleration generated by the structural deflection induced by traffic load is used to identify the curvature influence lines of the bridge, which are fused with modal estimates using a Kalman filter. The state variable of the analyzed system, representing a dense curvature profile of the structure subjected to concentrated loads, can be used as a damage-sensitive feature for high-resolution damage localization. The method is applied to a steel truss bridge subject to different damage configurations.

KEYWORDS: Kalman filter, influence line, modal curvature, structural health monitoring, damage identification.

Declaration of interests: The authors declare that they have no known competing financial interests or personal relationships that could have appeared to influence the work reported in this paper.

1. INTRODUCTION

Transport infrastructure ensures sustainable growth, social inclusiveness, and territorial cohesion. Roadway and railway bridges deserve special attention because of their number and function within the global

* Correspondence to: Said Quqa, Department DICAM, University of Bologna, Viale del Risorgimento 2, 40136 Bologna, Italy, e-mail: said.quqa2@unibo.it

E-mail addresses: said.quqa2@unibo.it (S. Quqa), l.landi@unibo.it (L. Landi).

transportation networks. Vibration-based structural health monitoring (SHM) can be beneficial for bridge managers to optimize maintenance and make appropriate decisions [1]. From this perspective, deploying sensing systems is crucial for making bridges safer.

In vibration-based SHM, modal parameters and derived quantities, such as modal flexibility [2] and curvature [3], are among the most popular damage-sensitive features (DSFs) due to their intuitive physical interpretability [4,5]. However, the possibility of identifying these features only at the instrumented locations makes dense sensor networks necessary to localize damage with satisfactory accuracy [6]. Moreover, approximated approaches used to calculate typical damage indicators based on curvature may amplify the effects of uncertainties of sparse modal parameters [7].

Damage localization using spatially sparse measurements has been typically achieved with the support of finite element (FE) models [8,9]. Nevertheless, generating and updating FE models can be laborious. Moreover, accurate geometrical details of the structure must be available, making the process particularly challenging for complex systems. Roving sensors [10] or instrumented vehicles [11,12] have also been employed to obtain dense structural features while using a modest number of sensing devices. However, these applications require operator inspections, which may be expensive and time-consuming, not allowing continuous monitoring. Recent studies processed the structural response collected through sparse sensors deployed on bridges traveled by moving vehicles to identify their influence lines. These features represent the variation of a given effect (typically displacement or strain) in a structural member due to a moving load as a function of its location.

Cavadas et al. [13] applied moving principal component analysis and robust regression analysis to the quasi-static displacement response of a bridge model traveled by moving loads to localize structural damage in an entirely data-driven approach. While the mentioned study considered filtering techniques to extract the quasi-static structural response, He et al. [14] used the displacement measurements of beam structures traveled by low-speed loads (below 1 m/s) to suppress the dynamic effects. The identified displacement influence lines were then used for damage localization. On the other hand, Zheng et al. [15] used displacement measurements induced by high-speed vehicles, eliminating the dynamic component through the empirical mode decomposition (EMD) [16]. Nevertheless, intrinsic mode functions (IMFs) obtained from different measurements may have different frequency content, thus needing a further selection algorithm to automatize the identification process [17]. Chen et al. [18] identified damage location and severity from displacement influence lines using prior knowledge of the structural stiffness retrieved from an updated numerical model. In general, displacement transducers and laser-based sensors can be expensive and need a fixed reference point, which is typically challenging to find in long-term field applications [19].

Strain measurements were also employed to identify strain and stress influence lines. Chen et al. [20] used the strain data collected during the passage of trains to determine the stress influence lines of railway bridges through regularization approaches, which also allowed identifying multiple damaged elements. Moreover, Frøseth et al. [21] used strain data of railway bridges to identify strain influence lines using deconvolution in the frequency domain. This method requires assuming a prior knowledge of the load pattern. Wang et al. [22] modeled the quasi-static and dynamic parts of the structural response using a piecewise polynomial and a series of harmonic sinusoids, respectively, which were employed to fit the dynamic structural response through a least-squares method. This method was used to extract displacement and strain influence lines from vehicle-induced vibration, forcing them to be piecewise cubic functions. Wu et al. [23] employed distributed strain data collected through long fiber Bragg grating sensors to identify damage in a continuous concrete girder bridge. In this case, the area of identified influence lines was used as a DSF. Although strain sensors are generally cheaper than displacement transducers, Alamdari et al. [24] showed that a dense sensor layout (i.e., several strain gauges or distributed sensing devices) is typically necessary to identify damage with a high resolution. The mentioned authors proposed a method to identify rotation influence lines considering only two instrumented locations deployed at the bridge bearings. This method was particularly effective for assessing cable losses in a cable-stayed bridge. However, the sensitivity of tiltmeters can be insufficient for small and stiff bridges. Huseynov et al. [25] used high-grade uniaxial accelerometers and the inverse sine transform to retrieve structural rotations. The difference in rotation influence lines obtained for healthy and damaged bridge

states was used as a damage indicator in the mentioned study. The authors noticed that, in general, sensors very close to the damage location were not particularly sensitive to damage, while the most convenient locations were at the supports. However, vibration amplitude at the support may be insufficient for low-cost instrumentation with a relatively high noise floor.

Cameras have also been employed to support or substitute other sensing devices. Zaurin et al. [26] integrated measurements from strain gages with camera recordings to correlate sensor data and vehicle locations for identifying strain influence lines. Martini et al. [27] exploited multiple camera measurements to obtain the geometric configuration of vehicle tire loads, their location on the bridge, and the structural displacement response at several target positions simultaneously, thus further limiting the sensing instrumentation. However, cameras must be deployed on fixed reference points, similar to displacement transducers.

In vibration-based SHM applications, accelerometers are still the most used sensors due to their simplicity of use. However, acceleration measurements have rarely been exploited to identify low-frequency traffic-induced effects on civil infrastructure. The primary issue, mainly related to traditional piezoelectric transducers, is that their operating bandwidth may exclude the quasi-static frequency range. However, recent force balance accelerometers (FBA) and micro-electromechanical system (MEMS)-based devices can collect dynamic recordings down to direct current (DC).

The authors of this paper recently conducted a proof-of-concept study to identify curvature influence lines of bridges only employing accelerometers [28]. Promising results showed that processing acceleration recordings collected during the passage of vehicles through simple filtering techniques provides curvature information with high spatial resolution. However, the results showed a high variance of the identified features due to the variability of the instantaneous signal amplitudes recorded during different vehicle passages (with varying speeds and positions on the deck). Also, a similar filtering scheme was applied to the same acceleration signals to identify modal parameters (i.e., natural frequencies and mode shapes), which showed more robustness compared to influence lines, as they were computed as an average estimate extracted on the entire time histories [29]. It was also shown that a unified monitoring approach based on a particular filter bank for extracting quasi-static and dynamic (modal) components could be employed to identify different structural features in a computationally convenient fashion [30]. However, using the identified structural parameters to obtain different damage indicators means conducting parallel damage identification processes, which may provide different results and generate confusion in structural condition assessment.

This paper presents a unified monitoring process for high-resolution damage localization, exploiting the robustness of modal parameters, which are defined only at sparse instrumented locations, and the spatial density of quasi-static features identified during vehicle passage, which, however, may be very sensitive to noise and transient phenomena. Therefore, the final goal of the proposed procedure is to obtain a single reliable and accurate DSF by fusing dynamic and quasi-static parameters obtained by sparse (and thus low-cost) instrumentation, which could be employed for monitoring minor bridges. Ultimately, analyzing the acceleration time histories collected on simply supported bridge decks while a vehicle travels with approximately constant speed, this method provides an estimate of the structural curvature when a set of concentrated loads are applied at the instrumented locations.

The main novelties introduced by this paper are the following:

1. An original procedure to identify dense structural curvature from acceleration data is proposed, which consists of fusing modal parameters and curvature influence lines through a Kalman filter, which also estimates the identification precision.
2. A novel strategy is introduced to remove flicker noise that may affect the low-frequency range of acceleration response using the EMD, which is very effective in the proposed framework due to the particular structure of the filtered acceleration signal.

Compared to state-of-the-art damage identification methods based on influence lines, the strategy proposed herein is only based on acceleration data, directly employed to calculate curvature based on a simple

physical rationale. Besides, compared to modal and flexibility curvature-based methods, this procedure is less sensitive to the errors that may derive from merely differentiating sparse mode shapes or derived quantities (e.g., those related to the central difference method [31]).

The proposed method is applied to acceleration measurements collected on a steel truss bridge tested with traffic-induced vibration under different real damage configurations. The analyses were conducted using different sensor layouts, proving that high-resolution damage localization can be achieved even using extremely sparse measurements.

2. IDENTIFICATION OF STRUCTURAL FEATURES

Vehicular traffic induces a variety of effects in the structural vibration response, namely (1) quasi-static effects due to the structural deflection under the weight of the passing vehicles; (2) dynamic effects due to the instantaneous equilibrium between inertial, elastic, and dissipative forces; (3) short-term effects mainly given by the interaction between the vehicle wheels and the uneven road surface.

Quasi-static effects are closely related to the instantaneous location of the vehicle and mainly affect the lowest (typically sub-hertz) frequency range in the spectrum of the structural response. On the other hand, dynamic effects can be modeled as the superposition of a set of vibration modes relevant to the structure, the vehicle, and their interaction. The first and most significant vibration modes populate the frequency range between a few hertz and a few dozen hertz for the most common viaducts. Finally, noise typically affects the entire spectrum, with most of its energy concentrated at the low (instrumental flicker noise) and high (road roughness effects) frequencies.

This section reports the theoretical background of the identification methods that can be employed to obtain dense curvature estimates from dynamic (modal) and quasi-static components of the structural vibration response. Moreover, a novel strategy is proposed to mitigate the effects of low-frequency instrumental noise. Throughout the paper, it is assumed that only accelerometers are employed to collect dynamic acceleration time histories of the structural response.

2.1 Structural response of a simply supported deck traveled by a vehicle

The acceleration signal in time t collected at a given section z of a bridge deck modeled as a one-dimensional simply supported beam, traveled by a vehicle having a weight P and a constant speed v can be represented as:

$$\ddot{u}(z,t) = \frac{\partial^2 u(z,t)}{\partial t^2} = \frac{P}{\mu}\delta(z - vt) - \frac{d}{\mu}\frac{\partial u(z,t)}{\partial t} - \frac{EI}{\mu}\frac{\partial^4 u(z,t)}{\partial z^4} \tag{1}$$

where $u(z,t)$ is the structural displacement, and the parameters μ, d, E, and I denote the mass per unit length, the damping coefficient, the elastic modulus of the material, and the inertia of the cross-section of the beam, respectively. Besides, in Equation (1), δ represents a Dirac delta function. Assuming a beam length equal to l, the application of P is bounded in the interval $t \in [0, l/v]$.

Assuming a linear-elastic structural behavior and the validity of the superposition principle, $\ddot{u}(z,t)$ can also be expressed as the linear combination of modal contributions:

$$\ddot{u}(z,t) = \sum_{m=1}^{\infty} \phi_m(z)\ddot{q}_m(t) \tag{2}$$

where $\phi_m(z)$ is the amplitude in z of the m-th mode shape of the structure, while $\ddot{q}_m(t)$ is the m-th modal acceleration response. In undamped cases, using a closed-form solution [32], Equation (2) can also be expressed as:

$$\ddot{u}(z,t) = -\frac{Pl^3}{48EI}\sum_{m=1}^{\infty}\frac{1}{m^2(m^2-\alpha^2)}sin\left(\frac{m\pi z}{l}\right)\left\{\left(\frac{m\pi v}{l}\right)^2\lambda_m(t)+\frac{\alpha}{m}p_m(t)\right\} \tag{3}$$

where $\lambda_m(t)$ and $p_m(t)$ represent the quasi-static and dynamic components of $\ddot{q}_m(t)$, respectively. The former is given by the deflection of the beam subject to the moving load P, applied statically. In Equation (3), the parameter α and the quasi-static component $\lambda_m(t)$ have the following expressions:

$$\alpha = \frac{vl}{\pi}\sqrt{\frac{\mu}{EI}} \tag{4}$$

$$\lambda_m(t) = sin\left(\frac{m\pi vt}{l}\right)\prod\left(\frac{vt}{l}-\frac{1}{2}\right) \tag{5}$$

with $\prod(t)$ denoting a rectangular function used to limit the support of $\lambda_m(t)$ to the load application interval. On the other hand, $p_m(t)$ is the impulse response of the structure relevant to the m-th mode, which has a frequency content condensed around the m-th damped circular frequency $\omega_{d,m}$ that, in the case of low damping, can be assumed as:

$$\omega_m = \frac{m^2\pi^2}{l^2}\sqrt{\frac{EI}{\mu}} \tag{6}$$

This study investigates damage localization along the longitudinal axis of the structure, i.e., z. However, in general, the bridge is a three-dimensional element, and vehicles move on the horizontal plane of the road. Specifically, different parallel lanes can be described using a further dimension in the equations above. Besides this, sensors are not generally deployed at the geometrical axis of the bridge in real setups, and their location can also be described using two (or three) coordinates. The concept of influence surface should be considered to take into account these aspects, making the analytical formulation more complex. However, a one-dimensional representation of the bridge can still be considered for the original purpose of this paper without affecting the results substantially (see Section 4.3 for more details).

2.2 Identification of curvature from modal parameters

Consider a set of natural frequencies ω_m and mode shapes $\phi_m(z_i)$, with $m = 1, \dots, M$ representing the number of identified modes and $i = 1, \dots, n$ the number of z_i instrumented locations, identified using a given modal identification algorithm. They can be organized in two matrices such that $\mathbf{\Lambda} = \text{diag}\{\omega_m^2\}$ and $[\mathbf{\Phi}]_{im} = \phi_m(z_i)$. Here, the operator diag{■} represents a diagonal matrix with the elements in its argument arranged on the main diagonal, while the notation $[■]_{ab}$ denotes the scalar element at the a-th row and b-th column of the matrix ■.

An estimate of the flexibility matrix of the monitored structure can be calculated as $\mathbf{F} = \mathbf{\Phi}\mathbf{\Lambda}^{-1}\mathbf{\Phi}^{\mathrm{T}}$. Besides, the deflection shape of the structure subjected to a set of unitary loads applied at the instrumented locations can be calculated as follows:

$$\mathbf{y} = \mathbf{F}\mathbf{p} = \mathbf{\Phi}\mathbf{\Lambda}^{-1}\mathbf{\Phi}^{\mathrm{T}}\mathbf{p} \tag{7}$$

with $\mathbf{p} = [1, \dots, 1]^{\mathrm{T}} \in \mathbb{R}^n$ representing the load vector. The vector $\mathbf{y}$ will be referred to as the uniform load line (ULL) vector hereafter. In order to calculate the actual flexibility matrix, mode shapes should be mass-normalized. However, normalized flexibility is not necessary for this study. Later in this paper, a normalization criterion will be shown to obtain a suitable proportional flexibility matrix for data fusion.

In the literature, the curvature is typically calculated using the central difference approximation directly on mode shapes or the ULL [33]. However, special care is required if sensors are not equally spaced. In this

case, a viable criterion is interpolating the identified modal amplitudes to a given function and then calculating its curvature. This study exploits the concept of shape functions typically employed in FE modeling. Equation (7) represents the structural deflection under a set of concentrated loads. Since a simply supported beam is considered in this paper, its bending moment (and curvature) diagram is piecewise linear. Assuming that curvature is the second derivative of displacement, the structural deflection can be effectively fitted using cubic polynomials, which have a linear second derivative. Specifically, a cubic spline is interpolated to the structural deflection $\mathbf{y}$ in this study. Thus, the curvature of the interpolating spline can be obtained by solving the following tridiagonal system [34]:

$$\mathbf{Uc} = \mathbf{d} \tag{8}$$

where $\mathbf{c} \in \mathbb{R}^n$ is the curvature at the spline knots, i.e., the instrumented locations, while $\mathbf{d} = \mathbf{VWy} \in \mathbb{R}^n$. In the case of a natural spline (i.e., with zero curvature values at the extrema), $\mathbf{U} \in \mathbb{R}^{n\times n}$ is defined as $[\mathbf{U}]_{im} = 2(\varepsilon_{i-1} + \varepsilon_i)$ if $i = m$, $[\mathbf{U}]_{im} = \varepsilon_i$ if $i = m - 1$, and $[\mathbf{U}]_{im} = \varepsilon_m$ if $i = m + 1$. Moreover, in this formulation, $\mathbf{W} \in \mathbb{R}^{n\times n}$ with $[\mathbf{W}]_{im} = -1/\varepsilon_i$ if $i = m$ and $[\mathbf{W}]_{im} = 1/\varepsilon_i$ if $i = m - 1$, except for $i = n$, where $[\mathbf{W}]_{im} = 0\ \forall m$, while $\mathbf{V} \in \mathbb{R}^{n\times n}$ with $[\mathbf{V}]_{im} = 6$ if $i = m$ and $[\mathbf{V}]_{im} = 6$ with $i = m + 1$, except for $i = 1$ and $i = n$, where $[\mathbf{V}]_{im} = 0\ \forall m$. These matrices can thus be represented in their extended forms as follows:

$$\mathbf{U} = \begin{bmatrix} 2\varepsilon_1 & 0 & 0 & \cdots & 0 & 0 & 0 \\ \varepsilon_1 & 2(\varepsilon_1+\varepsilon_2) & \varepsilon_2 & \cdots & 0 & 0 & 0 \\ 0 & \varepsilon_2 & 2(\varepsilon_2+\varepsilon_3) & \cdots & 0 & 0 & 0 \\ \vdots & \vdots & \vdots & \ddots & \vdots & \vdots & \vdots \\ 0 & 0 & 0 & \cdots & 2(\varepsilon_{n-3}+\varepsilon_{n-2}) & \varepsilon_{n-2} & 0 \\ 0 & 0 & 0 & \cdots & \varepsilon_{n-2} & 2(\varepsilon_{n-2}+\varepsilon_{n-1}) & \varepsilon_{n-1} \\ 0 & 0 & 0 & \cdots & 0 & 0 & 2\varepsilon_{n-1} \end{bmatrix} \tag{9}$$

$$\mathbf{W} = \begin{bmatrix} -\frac{1}{\varepsilon_1} & \frac{1}{\varepsilon_1} & 0 & \cdots & 0 & 0 \\ 0 & -\frac{1}{\varepsilon_2} & \frac{1}{\varepsilon_2} & \cdots & 0 & 0 \\ \vdots & \vdots & \vdots & \ddots & \vdots & \vdots \\ 0 & 0 & 0 & \cdots & \frac{1}{\varepsilon_{n-2}} & 0 \\ 0 & 0 & 0 & \cdots & -\frac{1}{\varepsilon_{n-1}} & \frac{1}{\varepsilon_{n-1}} \\ 0 & 0 & 0 & \cdots & 0 & 0 \end{bmatrix} \tag{10}$$

$$\mathbf{V} = \begin{bmatrix} 0 & 0 & 0 & \cdots & 0 & 0 & 0 \\ -6 & 6 & 0 & \cdots & 0 & 0 & 0 \\ 0 & -6 & 6 & \cdots & 0 & 0 & 0 \\ \vdots & \vdots & \vdots & \ddots & \vdots & \vdots & \vdots \\ 0 & 0 & 0 & \cdots & 6 & 0 & 0 \\ 0 & 0 & 0 & \cdots & -6 & 6 & 0 \\ 0 & 0 & 0 & \cdots & 0 & 0 & 0 \end{bmatrix} \tag{11}$$

with $\varepsilon_i = x_{i+1} - x_i$, and x_i represents the one-dimensional coordinate of the i-th instrumented location. The curvature $\mathbf{c}$ of the structure subjected to a given set of concentrated loads can thus be calculated from displacement values as:

$$\mathbf{c} = \mathbf{U^{-1}VWy} \tag{12}$$

In Equation (12), $\mathbf{c}$ is defined only at the instrumented locations. Due to the linearity of curvature in the studied case, the curvature can be calculated at a user-defined dense grid of N "inspection" locations ξ_j, with $j = 1, \dots, N$, using the following relation:

$$\hat{\mathbf{c}} = \mathbf{S}\mathbf{h} \tag{13}$$

where $\hat{\mathbf{c}} \in \mathbb{R}^{N\times 1}$ is the "extended" curvature vector, and $\mathbf{S} \in \mathbb{R}^{N\times n}$ is a block matrix for linear interpolation, defined as:

$$\mathbf{S} = \begin{bmatrix} \mathbf{S}_1 \\ \mathbf{S}_2 \\ \vdots \\ \mathbf{S}_{n-1} \end{bmatrix} = \begin{bmatrix} \frac{(x_2 - \xi_1)}{\varepsilon_1} & \frac{(\xi_1 - x_1)}{\varepsilon_1} & 0 & \cdots & 0 & 0 \\ \frac{(x_2 - \xi_2)}{\varepsilon_1} & \frac{(\xi_2 - x_1)}{\varepsilon_1} & 0 & \cdots & 0 & 0 \\ \vdots & \vdots & \vdots & & \vdots & \vdots \\ \frac{(x_2 - \xi_j)}{\varepsilon_1} & \frac{(\xi_j - x_1)}{\varepsilon_1} & 0 & \cdots & 0 & 0 \\ 0 & \frac{(x_3 - \xi_{j+1})}{\varepsilon_2} & \frac{(\xi_{j+1} - x_2)}{\varepsilon_2} & \cdots & 0 & 0 \\ 0 & \frac{(x_3 - \xi_{j+2})}{\varepsilon_2} & \frac{(\xi_{j+2} - x_2)}{\varepsilon_2} & \cdots & 0 & 0 \\ \vdots & \vdots & \vdots & \ddots & \vdots & \vdots \\ 0 & 0 & 0 & \cdots & \frac{(x_n - \xi_N)}{\varepsilon_{n-1}} & \frac{(\xi_N - x_{n-1})}{\varepsilon_{n-1}} \end{bmatrix} \tag{14}$$

with $b = 1, \dots, n-1$ indicating the block index, and $[\mathbf{S}_b]_{im} = (x_{b+1} - \xi_i)/\varepsilon_b$ if m is odd, while $[\mathbf{S}_b]_{im} = (\xi_i - x_b)/\varepsilon_b$ if m is even.

In summary, the extended curvature vector of the structure subjected to a set of unitary loads at the instrumented locations, defined at a dense spatial grid, can be calculated from modal estimates as follows:

$$\hat{\mathbf{c}} = \mathbf{S}\mathbf{U}^{-1}\mathbf{V}\mathbf{W}\mathbf{y} = \mathbf{S}\mathbf{U}^{-1}\mathbf{V}\mathbf{W}\boldsymbol{\Phi}\boldsymbol{\Lambda}^{-1}\boldsymbol{\Phi}^{\mathrm{T}}\mathbf{p} \tag{15}$$

Modal parameters have been largely employed in the last decades for SHM, and several algorithms exist for their identification in the time [35], frequency [5], and time-frequency [36] domain. Recently, an algorithm for identifying modal parameters in near-real-time was presented, which uses bandpass filters to extract the modal contributions included in the structural response, and can be employed to calculate instantaneous mode shapes and natural frequencies using nonlinear energy operators [29] or the Hilbert transform [37].

Assuming the use of a bandpass filter with impulse response $b_m[\tau]$ centered at the m-th natural frequency of the monitored structure, the dynamic part of the m-th modal contribution at the i-th instrumented location can be calculated as $\ddot{u}_m[z_i, t] = \ddot{u}[z_i, t] * b_m[\tau]$, where $*$ denotes the convolution operator. The instantaneous natural frequency of the relevant mode can be calculated using the Hilbert transform of $\ddot{u}_m[z_i, t]$. Also, an overall estimate of the natural frequency can be computed by averaging the identified instantaneous frequency over a user-defined time window. On the other hand, the instantaneous mode shape can be identified by calculating the ratio:

$$\phi_m[z_i, t] = \frac{\ddot{u}_m[z_i, t]}{\ddot{u}_m[z_r, t]} \tag{16}$$

where z_r is a reference instrumented location. Similar to natural frequencies, a more robust estimate of mode shapes can be calculated as the average of instantaneous values identified in a given time interval. It is worth noting that a preliminary estimate of the natural frequencies of the structure must be known *a priori* to design

suitable filters $b_m[\tau]$. This can be done by applying a simple peak-picking procedure to ambient vibration data collected before starting the long-term monitoring process. As an alternative, automatic methods exist to build suitable filter banks, which are not the focus of this paper. Thereby, the reader is remanded to [29,37] for more details on this topic.

It is worth noting that, in general, Equation (16) does not provide a mass-normalized estimate of **Φ**, which needs further normalization to obtain the real structural curvature. Mass information is typically hard to retrieve for existing structures. In this study, a normalization strategy is proposed to obtain realistic curvature estimates, as will be shown in Section (3.1). However, the mode shapes should be preliminarily normalized to a mass-proportional vector. If the monitored structure has a nearly constant cross-section or masses can be assumed as evenly distributed along the structural axis, mode shapes can be normalized to an identity matrix [29]. In this way, the matrix **F** can be considered proportional to the flexibility matrix of the structure.

2.3 Identification of curvature from quasi-static acceleration

Since the term $\lambda_m(t)$ of the structural response under moving loads does not include dynamic effects, the dependence of time in Equation (5) is only given by the varying location of the applied load. Thereby, the derivation variable can be easily changed with $\hat{z} = vt$, i.e., the space traveled by the passing vehicle. In this perspective, the quasi-static component of Equation (3) can be interpreted as a representation of the beam curvature in z (i.e., the double derivative in space of the deflection displacement) as a function of $\hat{z}$. This interpretation coincides with the definition of the curvature influence line of the beam calculated in the section z. Introducing the nondimensional variable $\zeta = z/l$, the curvature influence line of the beam calculated in the section ζ can be obtained analytically from Equations (3) and (5) as:

$$h^{(\zeta)}[\hat{z}] = -\frac{Pl^3}{48EI}\sum_{m=1}^{\infty}\frac{\pi^2 v^2\, sin(m\pi\zeta)}{l^2(m^2-\alpha^2)}sin\left(\frac{m\pi\hat{z}}{l}\right)\prod\left(\frac{\hat{z}}{l}-\frac{1}{2}\right) \tag{17}$$

This component is superimposed on the dynamic contributions in the structural response. However, the non-negligible components of the summation in Equation (17) are those with a low m index, and thus with a low frequency. Specifically, the most significant components of $h^{(\zeta)}[\hat{z}]$ typically populates the sub-hertz range of the structural response in the frequency domain. Also, for typical bridges and vehicle speed, α is generally very small. Neglecting its contribution, the first term of the summation in Equation (17) has an amplitude that is generally higher than 61% of the total amplitude of $h^{(\zeta)}[\hat{z}]$. This result comes from the Basel problem, according to which, $\sum_{m=1}^{\infty} 1/m^2 = \pi^2/6 \approx 1.64$, while the amplitude of the first component is 1. Similarly, the sum of the first four components in Equation (17) has an amplitude that is about 87% of the total amplitude of $h^{(\zeta)}[\hat{z}]$. Therefore, a good estimate of the quasi-static contribution can be extracted using a suitable lowpass filter with a cutoff frequency that includes the first terms of the summation in Equation (17). For instance, a cutoff frequency larger than $2v/l$ can be employed to extract the combination of the first four contributions. It is worth noting that the cutoff frequency should always be lower than the first natural frequency of the structure to avoid including dynamic contributions in the estimate of $h^{(\zeta)}[\hat{z}]$.

Adopting this criterion and assuming $b_0[\tau]$ as the impulse response of a suitable lowpass filter, the curvature influence line can be extracted from the acceleration response as:

$$h^{(\zeta)}[\hat{z}] \approx \left(\ddot{u}(z,t)|_{z=\zeta l,\ t=\hat{z}/v} * b_0\right)[\hat{z}] \tag{18}$$

Regarding the filter properties, the width of the transition band, the stopband attenuation, and the passband ripple influence the filtering outcome and depend on the filter order (and length). An attentive trade-off between filter performance and its length should be considered during filter design if the filtering task is carried out onboard smart sensing nodes to optimize the efficiency of edge computing. A recent study showed that the lowpass reverse biorthogonal wavelet filter with 3 vanishing moments has good selectivity and may be suitable for this task [30]. However, if the first natural frequency of the monitored structure is close to the cutoff

frequency of the lowpass filter, the side lobes in the frequency spectrum of $b_0[\tau]$ may include non-negligible dynamic components that contaminate the estimate of $h^{(\zeta)}[\hat{z}]$.

The side lobes of frequency-selective filters are typically well separated by high-attenuation regions. Therefore, if the same filter is applied to different intervals of the structural response, the dynamic effects selected by the side lobes have a similar pattern and generate contaminating components with well-separated frequency contents. This phenomenon makes the removal of dynamic effects included by side lobes particularly easy using the EMD [38]. This technique allows decomposing a given signal into different IMFs that generally span different frequency ranges. Such IMFs are characterized by the following properties: (1) the number of extrema and zero-crossings of each IMF must be equal or differ at most by one, and (2) at any point, the mean of the minima and maxima envelopes of each IMF must be zero [39]. Therefore, the signal can be expressed as a sum of IMFs plus a residual, which does not have the aforementioned properties. This decomposition can be applied to the identified influence lines as follows:

$$h^{(\zeta)}[\hat{z}] = \sum_{k=1}^{K} h_k^{(\zeta)}[\hat{z}] + r^{(\zeta)}[\hat{z}] \tag{19}$$

where $h_k^{(\zeta)}[\hat{z}]$ is the k-th IMF and $r^{(\zeta)}[\hat{z}]$ is the residual of $h^{(\zeta)}[\hat{z}]$. High-attenuation bands between lobes in the filtered structural response prevent mode-mixing in the formation of IMFs and guarantee that the quasi-static component selected by the main lobe and the dynamic components selected by the side lobes are divided into different IMFs. Thereby, this study proposes removing the first IMFs from the estimate of $h^{(\zeta)}[\hat{z}]$ to eliminate possible dynamic components and improve the readability of identified influence lines. In general, if the stopband attenuation is high or the natural frequency of the structure is far from the cutoff frequency, removing a single IMF is enough to improve the quality of identified features.

Besides dynamic components, flicker noise typically populates the low-frequency range of raw acceleration data, thus adding drifts to the extracted feature. For this reason, the EMD residual should also be removed from the identified influence line, obtaining:

$$\tilde{h}^{(\zeta)}[\hat{z}] = \sum_{k=2}^{K} h_k^{(\zeta)}[\hat{z}] \tag{20}$$

Due to the presence of the square function $\prod(t)$ in Equation (5), this estimate of $\tilde{h}^{(\zeta)}[\hat{z}]$ is only meaningful while the load is traveling on the monitored bridge span. For this reason, the identified feature should be cut (possibly, after filtering to avoid end effects [39,40]) at the instants where the vehicle enters and leaves the bridge. This process can be done with the help of optical sensors that collect the time references of these two instants or by observing the acceleration peaks of acceleration time history generated by the vehicle wheels hitting the expansion joints that divide simply supported bridge spans [28]. Moreover, the average vehicle speed can be identified from the length of the collected time history.

Due to the aforementioned properties of IMFs, the initial and last points of $\tilde{h}^{(\zeta)}[\hat{z}]$ are generally different from zero. However, the curvature at the supports should be null due to the static properties of the simply supported beam. In order to fix this issue, a linear trend can be removed from $\tilde{h}^{(\zeta)}[\hat{z}]$, obtaining:

$$\bar{h}^{(\zeta)}[\hat{z}] = \tilde{h}^{(\zeta)}[\hat{z}] - \tilde{h}^{(\zeta)}[0] - \frac{\tilde{h}^{(\zeta)}[L] - \tilde{h}^{(\zeta)}[0]}{L}\hat{z} \tag{21}$$

where L is the number of samples of the identified influence line.

Although this study assumes that the vehicle speed is constant in a given recording (typically the case for bridges with a length up to 50-100 m in light traffic conditions), different vehicles may have different average speeds. Since the sampling rate of the accelerometers is always constant during the monitoring process, the

length of $h^{(\zeta)}[\hat{z}]$ is variable. Therefore, interpolating the identified influence line to a user-defined fixed spatial greed is necessary for further processing. Specifically, for the aims of this paper, the inspection grid introduced in Section 2.2 with N locations should be used for interpolation.

It is worth noting that, potentially, the EMD could be used directly on the raw vibration data for extracting the influence line [15]. However, IMFs obtained from different acceleration time histories may be numbered differently based on disturbing factors or nonstationary components. This phenomenon would make automatic signal processing challenging [17]. Furthermore, the high-attenuation regions in the filtered response spectra minimize the occurrence of mode mixing issues.

3. FEATURE FUSION AND DAMAGE IDENTIFICATION

This study aims to fuse the ULLs obtained from modal parameters, as explained in Section 2.2, with dense curvature estimates identified from accelerations recorded during the passage of vehicles, as shown in Section 2.3. This is achieved using a Kalman filter (KF). However, preliminary data normalization is necessary to make the two estimates consistent.

3.1 Feature normalization

The feature obtained from Equation (18) represents a curvature estimate but physically is an acceleration. The first step for data normalization is thus finding a scale factor $a_M^{(\zeta)}$ that transforms the acceleration sequence $\bar{h}^{(\zeta)}[\zeta l]$ into a curvature sequence $c^{(\zeta)}[\zeta l]$ with suitable physical dimension (the inverse of a length).

As already mentioned in Section 2.3, for ordinary bridges and vehicle speed, $\alpha^2 \ll 1$. Thereby, the maximum of the identified influence line (which is at $\hat{z} = \zeta l$ for a simply supported beam, with ζ indicating the instrumented location) can be calculated from Equation (17) as follows:

$$\max\left(\bar{h}^{(\zeta)}\right) = \bar{h}^{(\zeta)}[\zeta l] \approx \frac{\pi^2 v^2 P l s_M^{(\zeta)}}{48EI} \tag{22}$$

where $s_M^{(\zeta)}$ is a parameter that only depends on the instrumented location and the cutoff frequency of the lowpass filter. Indeed, M is the number of quasi-static components in the summation of Equation (17) included in the passband of the filter. The term $s_M^{(\zeta)}$ is thus defined as:

$$s_M^{(\zeta)} = \sum_{m=1}^{M} \frac{sin(m\pi\zeta)^2}{m^2} \tag{23}$$

The theoretical curvature maximum of a simply supported beam loaded at $\hat{z} = \zeta l$ can also be calculated as:

$$c^{(\zeta)}[\zeta l] = \frac{P l \zeta (1-\zeta)}{EI} \tag{24}$$

Therefore, the scale factor that transforms $\bar{h}^{(\zeta)}[\zeta l]$ into $c^{(\zeta)}[\zeta l]$ can be calculated as the ratio between Equations (22) and (24):

$$a_M^{(\zeta)}(v) = \frac{\bar{h}^{(\zeta)}[\zeta l]}{c^{(\zeta)}[\zeta l]} = \frac{\pi^2 s_M^{(\zeta)}}{48\zeta(1-\zeta)} v^2 \tag{25}$$

which depends on the vehicle speed, instrumented location, and filter cutoff frequency. Figure 1 reports $s_M^{(\zeta)}$ and $a_M^{(\zeta)}/v^2$ for different values of ζ and M.

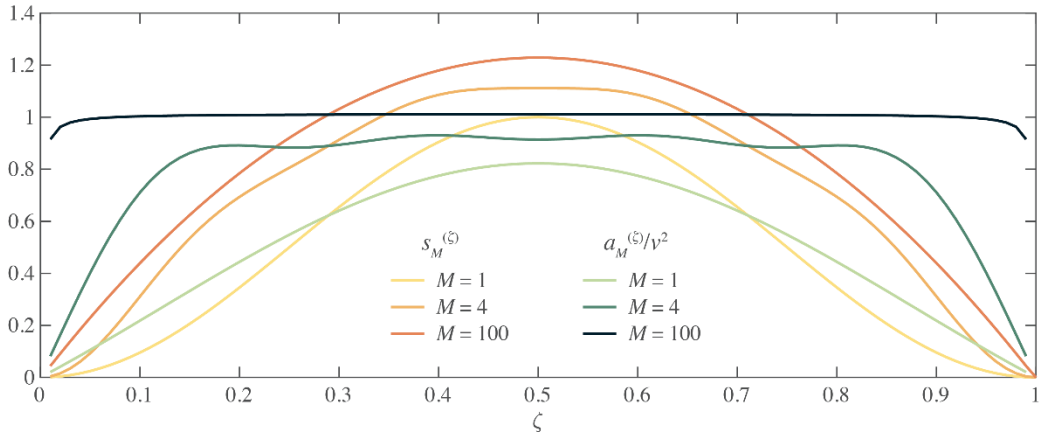

Figure 1 – Scale factors for influence line scaling

For linear-elastic and statically determined structures, according to the Maxwell-Betti theorem, the influence line of a given effect calculated in a section of the structure is equal to the relevant deformed shape of the structure subject to a concentrated load applied at that section. Therefore, the calculated influence line can also be interpreted as the curvature diagram of the structure (proportional to the bending moment diagram) generated by a force applied at the instrumented location. Multiple influence lines can thus be summed by exploiting the superposition principle, obtaining the curvature diagram of the structure subjected to a set of uniform concentrated loads applied at all the instrumented locations, as follows:

$$\bar{c}[\hat{z}] = \sum_{i=1}^{n} \frac{\bar{h}^{(\zeta_i)}[\hat{z}]}{a_M^{(\zeta_i)}} \tag{26}$$

This result is equivalent to the outcome of Equation (15) obtained from modal parameters, except for a scaling factor. The elements of $\bar{c}[\hat{z}]$ can be arranged in a column vector $\bar{\mathbf{c}} \in \mathbb{R}^N$ to facilitate feature fusion through the KF.

With mass-normalized mode shapes, Equation (7) can be used to obtain the displacement profile of the structure subjected to a set of unitary loads applied at the instrumented locations. However, the curvature estimates of Equation (21) obtained from the quasi-static structural response also contain information about the vehicle weight. Thereby, in general, in order to make the two estimates comparable, both the vehicle load and the structural masses should be known. Alternatively, the use of masses can be avoided by directly scaling the displacement profile $\mathbf{y}$ to an expected profile obtained by knowing the structural scheme and its stiffness. This can be done assuming that the cross-section of the structure is constant and an inspection vehicle with known weight is used at the beginning of the monitoring process. In this case, Equation (22) can be inverted to evaluate the flexural stiffness of the bridge deck (or an equivalent quantity if the structure has a non-uniform cross-section). For instance, using an accelerometer deployed at the midspan ($\zeta = 1/2$) and a filter such that $M = 4$, the flexural stiffness can be estimated as:

$$EI \approx 0.228 \frac{v^2 P l}{\bar{h}^{(1/2)}[l/2]} \tag{27}$$

Using this estimate, the displacement profile can thus be normalized as follows:

$$\bar{\mathbf{y}} = \frac{Pl^3}{3EI} \frac{(\zeta_i^2 - \zeta_i)^2}{y_i[i]} \mathbf{y} \tag{28}$$

where $y_i[i]$ is the i-th element of the vector $\mathbf{y}_i = \mathbf{\Phi}\mathbf{\Lambda}^{-1}\mathbf{\Phi}^{\mathrm{T}}\mathbf{p}_i$ and $\mathbf{p}_i$ is a zero-valued column vector with the i-th element equal to 1.

After obtaining an estimate of EI, since the vehicle weight is unknown during the ordinary monitoring phase, Equation (27) can be inverted to obtain P for each vehicle run and apply the normalization criterion of Equation (28) to the following identified ULLs. It is worth noting that, in contrast to the dense of curvature estimates, for which every $\bar{h}^{(\zeta_i)}[\hat{z}]$ needs to be normalized using a different scale factor that depends on the instrumented location, Equation (28) can be applied using any i value.

3.2 Feature fusion

For feature fusion, the discrete-time KF is employed in this study. Specifically, the state variables are defined as the real curvature values of the bridge deck at the user-defined dense grid of inspection locations defined in Section 2. The state vector at the k-th inspection instant is indicated as $\boldsymbol{\chi}_k$. This vector is updated using the KF at every new inspection, i.e., as soon as a new set of modal parameters or dense curvature estimates is available.

Since damage is not expected to occur in ordinary situations, the state transition model, i.e., the evolution of $\boldsymbol{\chi}_k$ between the $(k-1)$-th and k-th instants is assumed as a "random walk" model, i.e., with a state transition matrix equal to the identity matrix ($\mathbf{I}$), considering the uncertainty given by a normally-distributed process noise vector $\mathbf{w}_k \sim \mathcal{N}(\mathbf{0}, \mathbf{Q}_k)$ with zero mean and covariance matrix $\mathbf{Q}_k$. Therefore, the state transition model reads:

$$\boldsymbol{\chi}_{k+1} = \mathbf{I}\boldsymbol{\chi}_k + \mathbf{w}_k \tag{29}$$

Depending on the available measurement (here indicated with the vector $\mathbf{z}_k$), the observation model is different. Specifically, if the new measurement consists of a set of modal parameters, they are first used to calculate the ULL, which is then used as input to update the state of the system. In this case ($\mathbf{z}_k = \bar{\mathbf{y}}$), the observation model reads:

$$\bar{\mathbf{y}} = (\mathbf{S}\mathbf{U}^{-1}\mathbf{V}\mathbf{W})^{\dagger}\boldsymbol{\chi}_k + \mathbf{v}_k^{\mathrm{UL}} \tag{30}$$

where $\blacksquare^{\dagger}$ denotes the Moore-Penrose pseudoinverse of the marix $\blacksquare$. On the other hand, if a new estimate of dense curvature is available ($\mathbf{z}_k = \bar{\mathbf{c}}$), the observation model is represented by the equation:

$$\bar{\mathbf{c}} = \mathbf{I}\boldsymbol{\chi}_k + \mathbf{v}_k^{\mathrm{IL}} \tag{31}$$

In Equations (30) and (31), the measurement noise vectors of the ULL and dense curvature estimate obtained from the influence lines, $\mathbf{v}_k^{\mathrm{UL}} \sim \mathcal{N}(\mathbf{0}, \mathbf{R}^{\mathrm{UL}})$ and $\mathbf{v}_k^{\mathrm{IL}} \sim \mathcal{N}(\mathbf{0}, \mathbf{R}^{\mathrm{IL}})$, respectively, are assumed as time-invariant, i.e., they do not depend on the inspection time.

The KF operates through two recursive steps: the prediction and update steps, which alternate. The former step uses the quantities identified up to the $(k-1)$-th instant to predict the state at the k-th instant and the associated covariance matrix $\mathbf{P}_k$. This step is represented by the following relations:

$$\hat{\boldsymbol{\chi}}_{k|k-1} = \hat{\boldsymbol{\chi}}_{k-1|k-1} \tag{32}$$

$$\mathbf{P}_{k|k-1} = \mathbf{P}_{k-1|k-1} + \mathbf{Q}_{k-1} \tag{33}$$

Here $\hat{\boldsymbol{\chi}}_k$ indicates an estimate of $\boldsymbol{\chi}_k$, and the notation $\hat{\boldsymbol{\chi}}_{k|k-1}$ indicates the estimated state vector at the k-th instant considering the measurements obtained up to the $(k-1)$-th instant.

The update step involves the calculation of the Kalman gain $\mathbf{K}_k$ and the update of the state vector and covariance using a new measurement. It can be carried out by calculating the following quantities:

$$\mathbf{K}_k = \mathbf{P}_{k|k-1}\mathbf{H}_k^{\mathrm{T}}\left(\mathbf{H}_k\mathbf{P}_{k|k-1}\mathbf{H}_k^{\mathrm{T}} + \mathbf{R}_k\right)^{-1} \tag{34}$$

$$\hat{\boldsymbol{\chi}}_{k|k} = \hat{\boldsymbol{\chi}}_{k|k-1} + \mathbf{K}_k\left(\mathbf{z}_k - \mathbf{H}_k\hat{\boldsymbol{\chi}}_{k|k-1}\right) \tag{35}$$

$$\mathbf{P}_{k|k} = (\mathbf{I} - \mathbf{K}_k\mathbf{H}_k)\mathbf{P}_{k|k-1} \tag{36}$$

In these equations, $\mathbf{H}_k = (\mathbf{S}\mathbf{U}^{-1}\mathbf{V}\mathbf{W})^{\dagger}$ if $\mathbf{z}_k = \bar{\mathbf{y}}$, while $\mathbf{H}_k = \mathbf{I}$ if $\mathbf{z}_k = \bar{\mathbf{c}}$. Besides, the measurement noise covariance $\mathbf{R}_k$ is selected accordingly for each update. For initializing the KF, the initial state can be set as $\hat{\boldsymbol{\chi}}_{0|0} = \mathbf{S}\mathbf{U}^{-1}\mathbf{V}\mathbf{W}\bar{\mathbf{y}}$, using the first estimate of $\bar{\mathbf{y}}$ (see Equation 15) and the initial state covariance $\mathbf{P}_{0|0}$ can be assumed as a diagonal matrix with non-zero elements in the order of the diagonal elements of $\mathbf{R}^{\mathrm{IL}}$.

3.3 High-resolution damage localization

This study considers the updated estimate of the curvature $\hat{\boldsymbol{\chi}}_{k|k}$ as a dense DSF which is representative of the structural stiffness. Thereby, a damage index at the instant k can be defined as the difference

$$\Delta\hat{\boldsymbol{\chi}}_k = \hat{\boldsymbol{\chi}}_{k|k} - \hat{\boldsymbol{\chi}}_{\beta|\beta} \tag{37}$$

between the estimate at the inspection instant and a baseline estimate $\hat{\boldsymbol{\chi}}_{\beta|\beta}$. It is also possible to determine the variance of the damage indicator, which can be interpreted as a quality index of the damage estimate, as:

$$\boldsymbol{\sigma}_k^2 = \mathrm{diag}\left(\mathbf{P}_{k|k} + \mathbf{P}_{\beta|\beta}\right) \tag{38}$$

Specifically, the precision of an estimate can be calculated as the inverse of its variance. Thereby, local precision parameters can be calculated as $1/\boldsymbol{\sigma}_k^2$ for all the points of the inspection grid.

The instant β where the baseline condition is selected should be assumed when the values of $\mathbf{P}_{k|k}$ become stable with increasing updates, i.e., when

$$\left\|\mathrm{diag}\left(\mathbf{P}_{k|k} - \mathbf{P}_{k-1|k-1}\right)\right\| \leq \eta \tag{39}$$

with η a user-defined parameter. Therefore, observing the evolution of $\mathrm{diag}\left(\mathbf{P}_{k|k}\right)$ in time is helpful to select a suitable baseline for damage identification when the state variance is low.

In summary, the entire identification method proposed in this paper is schematized in Figure 2. A preliminary initialization phase is carried out to build the bandpass filters based on the resonant frequencies of the structure to extract the relevant mode shapes. Then, the acceleration time histories collected during a vehicle passage are filtered using both the lowpass and bandpass filters to obtain influence lines and mode shapes, respectively. From these features, a dense curvature profile and a sparse displacement profile of the structure subjected to concentrated loads at the instrumented locations are calculated and fused into a robust curvature estimate through the KF, upon normalization. Then, monitoring the state evolution over time allows for identifying localized stiffness variations with high resolution.

The method proposed in this paper can be applied to different types of simply supported bridges. While it assumes that (1) instrumented locations and vehicle loads are on the geometrical axis of the bridge, and (2) the structure has a constant cross-section, acceptable identification results can also be obtained for more general cases in which these assumptions are not strictly verified. Section 4 presents real and simulated applications relevant to a steel truss bridge with a varying cross-section and eccentric sensors and loads.

The method can also be used for reinforced concrete bridges, which typically have a constant cross-section (e.g., prestressed overpasses). In the proposed formulation, Equation (1) does not explicitly include prestressing forces. Since the damage indicator employed in this study is based on curvature difference, the authors believe that the curvature variation due to prestress losses (which generally manifest in the long term)

would not affect the capability of the algorithm to quantify localized anomalies. Indeed, in general, prestressed elements have a fully compressed cross-section. Modest prestress force losses not leading to material cracking do not modify the section stiffness. On the other hand, if prestress forces become very low, the effective compressed section may reduce, thus involving a local stiffness reduction that can be identified through the proposed method [41]. The effect of prestressing forces needs to be analyzed in detail in future studies.

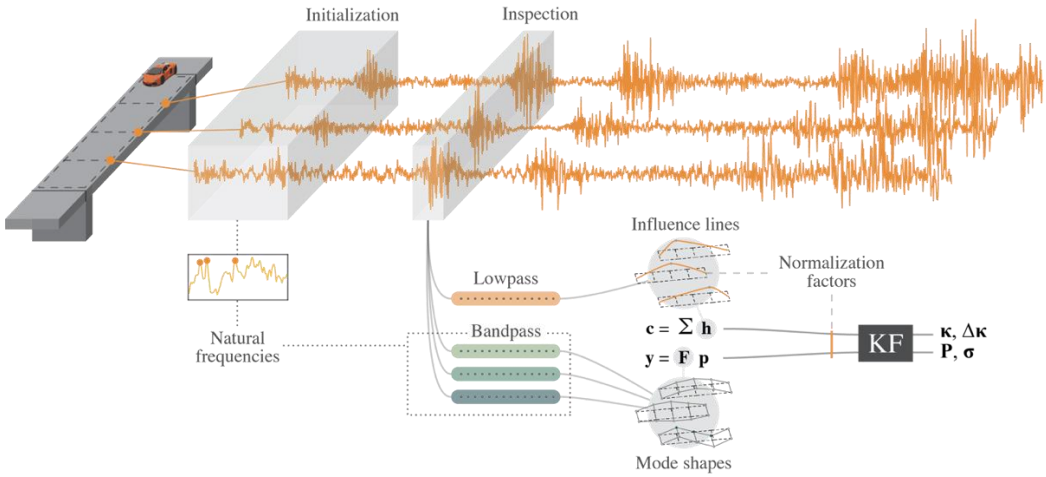

Figure 2 – Scheme of the proposed identification procedure

4. APPLICATIONS

The monitoring approach proposed in the previous sections is herein applied for damage localization in a real steel truss bridge. Both experimental and simulated data are employed in this section. The latter is obtained using a finite element model built according to the geometry of the real bridge. Two sensor setups are considered to investigate the quality of identification results with different levels of sparsity. Before discussing the results, a brief description of the case study is provided.

4.1 Description of the case study

The Old ADA Bridge (Figures 3 and 4) was built in 1959 in Japan and demolished in 2012 after conducting an experimental campaign aimed at collecting ambient and vehicle-induced vibration data under different damage configurations. The structure consisted of two lateral steel Warren trusses supporting a steel and RC deck. The span length and deck widths were 59.2 m and 3.6 m, respectively. The thickness of the RC deck was 210 mm, and the steel elements had I, T, and box sections, described in detail in [42].

Published in *Mechanical Systems and Signal Processing*
Volume 186, March 2023, Article 109907. https://doi.org/10.1016/j.ymssp.2022.109907

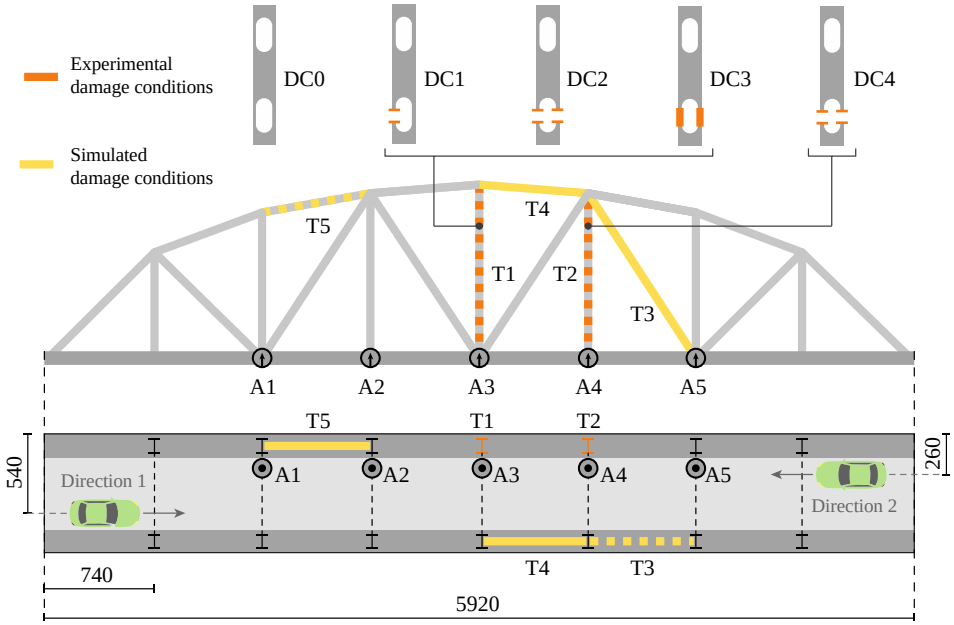

Figure 3 – Scheme of the case study, sensor layout, and damage configurations; adapted from [42], *units in cm.*

Experimental tests were conducted before demolition [43]. During the tests, traffic was blocked to deploy a sensor network of 8 accelerometers on the bridge deck and use a single test vehicle to excite the bridge (Nissan Serena, with an approximate total weight of 21 kN, shown in Figure 4c). The front and back wheel axles of this vehicle were 2.7 m distant, while the track width was 1.5 m. The authors who conducted the tests identified the first resonant frequency of the vehicle at 1.7–1.8 Hz. On the other hand, the first five identified resonant frequencies of the bridge were 2.975 Hz, 6.872 Hz, 9.608 Hz, 10.559 Hz, and 13.418 Hz [44].

The accelerometers used to collect vibration data in the vertical direction (sampled at 200 Hz) were produced by Tokyo Measuring Instruments (ARS-A model) and have a nominal responding frequency from DC to 30 Hz. Acceleration data collected in ambient and traffic conditions are freely available in an online repository [43]. In this study, only the data collected by five accelerometers deployed in a line, as shown in Figure 3, have been considered.

During the tests, four damage scenarios were induced artificially. First, the central vertical truss element (T1) at one side of the deck was reduced by half (Figure 4d). This structural configuration will be referred to as “DC1” in this paper. Then, the same truss element was completely cut (configuration “DC2”), as shown in Figure 4e. The central truss element was then repaired by soldering the damaged element (Figure 4f) after lifting the bridge to the original position (“DC3”). Afterward, the element T2 was damaged by completely cutting the element (“DC4”). In this study, the condition “DC0” represents the “undamaged” configuration before inducing the first damage.

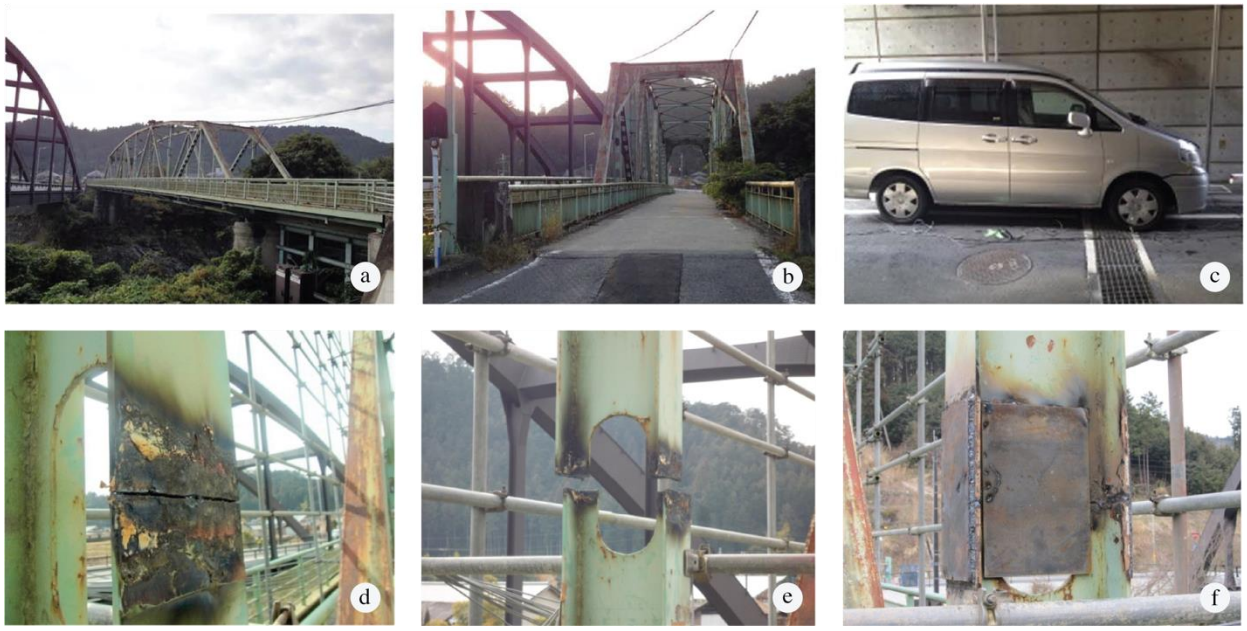

Figure 4 – Pictures of the old ADA Bridge [42,44]*: (a) side view, (b) front view, (c) vehicle used for dynamic tests, (d) partial cut of the damaged element, (e) total cut of the damaged element, (f) retrofit of the damaged element*

In each configuration (from DC0 to DC4), different time histories of ambient and vehicle-induced vibration data were collected using the accelerometers deployed. For the latter test type, three different vehicle speeds were used in configuration DC0 (i.e., 30, 40, and 50 km/h), while vibration data were only collected with the vehicle traveling at 40 km/h in the other configurations. During these tests, the vehicle was moving in Direction 1 (see Figure 3). The exact location of the vehicle was not specified in the dataset documentation. Moreover, three optical sensors (PZ-G52 by Keyence Co.) were used to track the time when the vehicle passed on the bridge supports and the midspan. No substantial temperature change was observed during the tests.

In this study, an FE model of the bridge was built according to the geometry details given in [42]. Beam elements were used for the truss structure, the bracing, and the floor beams, while shell elements were modeled to simulate the RC deck. The first five natural frequencies of the simulated structures were 2.958 Hz, 7.005 Hz, 9.821 Hz, 10.673 Hz, and 13.227 Hz, with an average absolute error of 1.41% with respect to the experimental results mentioned above. In this simulation, absolute acceleration data were generated at the nodes A1 and A5 of the scheme reported in Figure 3 during the passage of one concentrated moving load along two different axes and in two different directions, simulating the passage of a vehicle in different lanes. Specifically, the first lane was modeled considering a horizontal axis distant 5.4 m from the instrumented edge, with the vehicle moving in Direction 1 (see Figure 3). On the other hand, the second lane was modeled considering a horizontal axis distant 2.6 m from the instrumented edge, with the vehicle moving in Direction 2. Three incremental damage conditions were simulated in the FE model, reducing by 10% the cross-sectional areas of elements T3 (condition DCs1), T3 and T4 (condition DCs2), and T3, T4, and T5 (condition DCs3). The results of this simulation are commented on in Section 4.3, while Section 4.2 reports and discusses the results obtained using the experimental data.

4.2 Discussion of the experimental results

In this study, 55 experimental acceleration datasets (15 in configuration DC0 and 10 in DC1, DC2, DC3, and DC4) were used to apply the proposed identification method. Each dataset consists of acceleration time histories with a duration of about 45 s, collected at all the instrumented locations during the vehicle passage. 50 datasets were collected with the vehicle passing at 40 km/h (10 for each damage configuration), while 5 additional datasets were collected with the vehicle passing at 50 km/h in DC0. These last records were only used to validate the scaling factors, as will be shown later.

Each dataset represents an inspection, in which a set of modal parameters (natural frequencies and mode shapes) and curvature influence lines were identified using the procedures presented in Sections 2.2 and 2.3. Specifically, a bank of five filters was employed to decompose the acceleration signal at all the instrumented locations. The first filter of the bank is a lowpass filter obtained by cascading 8 reverse biorthogonal wavelet lowpass filters with three vanishing moments (*rbio3.1*) [45]. The resulting equivalent filter is thus a lowpass filter with a cutoff frequency of $F_s/2^9$, where F_s is the sampling frequency of the signal. Considering F_s = 200 Hz, the cutoff frequency of the lowpass filter is 0.39 Hz. The other filters of the bank are bandpass filters obtained by cascading eight Fejér-Korovkin wavelet lowpass and highpass filters with four vanishing moments (*fk4*) [46] to obtain equivalent bandpass filters with a narrow passband (0.39 Hz wide), each including one resonant frequency of the structure [30]. It is worth noting that the bandpass filters can be built by changing the cascading order based on the natural frequencies of the structure, which must be known *a priori* (e.g., by applying a simple peak-picking procedure on ambient vibration data collected before starting the long-term monitoring process).

According to Equation (18), the outcome of the lowpass filter is an estimate of the curvature influence calculated at the instrumented location, which must be further processed through the EMD to obtain the result reported in Equation (21).

On the other hand, the outcome of the m-th bandpass filters represents $\ddot{u}_m[z_i, t]$ in Equation (16), which can be employed to obtain the instantaneous mode shapes of the structure in the inspection window. As mentioned in Section (2.2), the instantaneous mode shapes can be averaged to obtain a more robust estimate, which can thus be processed to obtain the ULL $\mathbf{y}$. In this application, the first four modes of the structure preliminarily identified by Kim et al. [42] were tracked during the following monitoring process.

Upon filtering, the output of the lowpass filter was cut at the instants identified through the optical sensors when the vehicle entered and left the bridge. On the other hand, full time histories resulting from the bandpass filter of about 45 s containing the effects of vehicle passage and the following free-response vibration were used to identify modal parameters.

At the beginning of the monitoring process, the scale factors for both the ULLs and the influence lines must be determined. Equation (27) was first applied to a set of 10 influence lines identified at the midspan in configuration DC0 (5 with a vehicle speed of 40 km/h and 5 with a vehicle speed of 50 km/h). In this initialization phase, the vehicle weight was assumed as known, simulating the use of an inspection car. The average maxima of the identified influence lines were $\bar{h}^{(1/2)}[l/2] = 0.0024\ m/s^2$ for the lower speed and $\bar{h}^{(1/2)}[l/2] = 0.0039\ m/s^2$ for the higher speed recordings, resulting in $EI \approx 1.4581 \cdot 10^7 kN \cdot m^2$ and $EI \approx 1.4778 \cdot 10^7 kN \cdot m^2$, respectively. The low variability of these results obtained for two different speeds confirms the robustness of the estimate.

The identified flexural stiffness was thus employed to normalize the ULLs using Equation (28). On the other hand, individual influence lines are scaled using the coefficients defined in Equations (23) and (25). For this case study, the cutoff frequency of the lowpass filter includes the first four components of $s_M^{(\zeta)}$; thereby, in this case, $M = 4$. The values of the scale factors calculated at the instrumented locations are reported in Table 1.

Table 1 – Scale coefficients at the instrumented locations for M = 4

ζ	1/4	3/8	1/2
$s_4^{(\zeta)}$	0.806	1.057	1.111
$a_4^{(\zeta)}/v^2$	0.883	0.928	0.914

4.2.1 Full sensor setup

First, the results obtained using the full sensor setup (i.e., A1, A2, A3, A4, and A5) are presented. In this case, the scaled influence lines identified at all locations were summed to obtain the curvature of the structure

subjected to a uniform set of concentrated loads applied at the instrumented locations, according to Equation (26).

In this study, a monitoring process is simulated with periodic inspections. The 50 datasets collected from DC0 to DC4 are thus assumed as consecutive inspections (10 for each damage configuration) carried out during a monitoring period. In this period, different damaging events occur, as well as a retrofit intervention between DC2 and DC3. The scaled ULLs and dense curvature estimates obtained in the different inspections are reported in Figure 5. These parameters have a color from light green (DC0) to dark green (DC4), which changes as a function of the inspection time.

It is worth noting that the ULLs are only defined at the instrumented locations (indicated as vertical dashed lines in Figure 5). Therefore, the displacement profile between different estimates is piecewise linear. Although the robustness of these estimates is higher, as a single set of modal parameters is obtained from a set of acceleration time histories with a relatively long duration (i.e., about 45 s), observing the ULLs would not allow accurately localizing concentrated defects. On the other hand, the curvature profiles obtained from influence lines are represented by the instantaneous filtered acceleration of the structure, thus showing more variability depending on the specific vehicle speed and path, as well as the recording noise. Specifically, the time histories used to identify influence lines are about 5 s long, as they are limited to the time interval in which the vehicle is on the bridge.

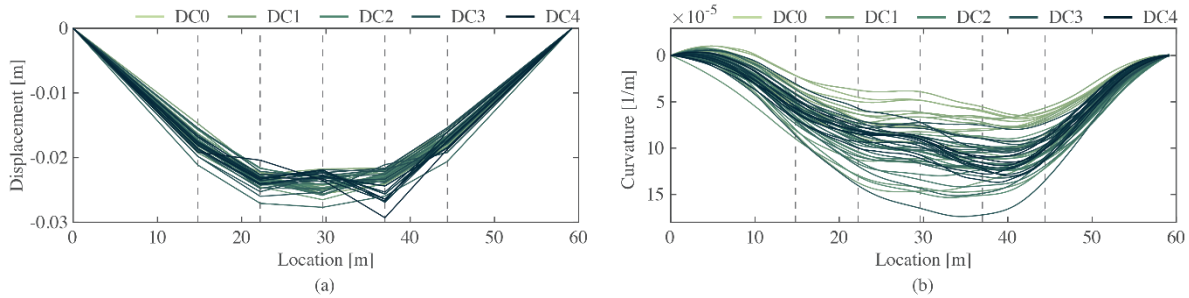

Figure 5 – Identified parameters: (a) uniform load lines from modal parameters, (b) dense curvature profiles from quasi-static structural response

The KF was thus employed to fuse these two features to obtain dense and robust estimates of the structural curvature, together with the relevant covariance matrix. In order to initialize the KF, the initial state was selected as $\hat{\boldsymbol{\chi}}_{0|0} = \mathbf{S}\mathbf{U}^{-1}\mathbf{V}\mathbf{W}\bar{\mathbf{y}}$, while the initial state covariance matrix was set as $\mathbf{P}_{0|0} = \mathbf{R}^{\mathrm{IL}}$, where $\mathbf{R}^{\mathrm{IL}}$ is the noise covariance matrix of the dense curvature profile. This matrix was set as a diagonal matrix with constant non-zero elements equal to the mean of the diagonal of the covariance matrix obtained from 10 estimates of the dense curvature profile identified in DC0. The result of this operation is $\mathbf{R}^{\mathrm{IL}} = 4.85 \cdot 10^{-7}\mathbf{I}\, m^2$. Similarly, $\mathbf{R}^{\mathrm{UL}} = 1.25 \cdot 10^{-10}\mathbf{I}\, m^{-2}$ was obtained as the mean of the diagonal of the covariance matrix obtained from 10 ULL estimates identified in DC0.

The process noise covariance matrix determines the uncertainty level of the process model. The larger the values in $\mathbf{Q}$, the higher the uncertainty and the faster the state adapts to the measurements. If the initial state is different from the following measurements, a variable (depending on the magnitude of $\mathbf{Q}$) time interval from initialization is necessary for the state to stabilize. The baseline condition for damage identification should not be taken in this interval, as residual curvature differences due to state adaptation may lead to false positives in the monitoring process. Figure 6 shows (a) the KF state, (b) the damage indicator defined in Equation (37), and (c) the variance of the state estimates. These results are obtained for two different process noise matrices. Specifically, the figures on the left-hand side are obtained using $\mathbf{Q} = \mathbf{R}^{\mathrm{UL}}/10$, while the ones on the right-hand side are obtained using $\mathbf{Q} = \mathbf{R}^{\mathrm{UL}}/100$. As expected, the updated states and damage indicators have a higher variance in the first case, as the incidence of measurements on updates is higher. On the other hand, lower process noise leads to more robust estimates, which have a slower stabilization, as shown in Figure 6c.

These results included an initial monitoring phase in which the states and relevant covariance stabilize by repeating the inspection carried out in DC0 twice. Indeed, Figures 6a and 6c represent 60 inspections (a set of 10 inspections in DC0 for initialization and a set of 50 inspections from DC0 to DC4 representing the regular monitoring process). The baseline state for damage identification was selected as $\hat{\boldsymbol{\chi}}_{10|10}$, when identification precision was almost stable. After this instant, 50 estimates of the damage index were computed (reported in Figure 6b).

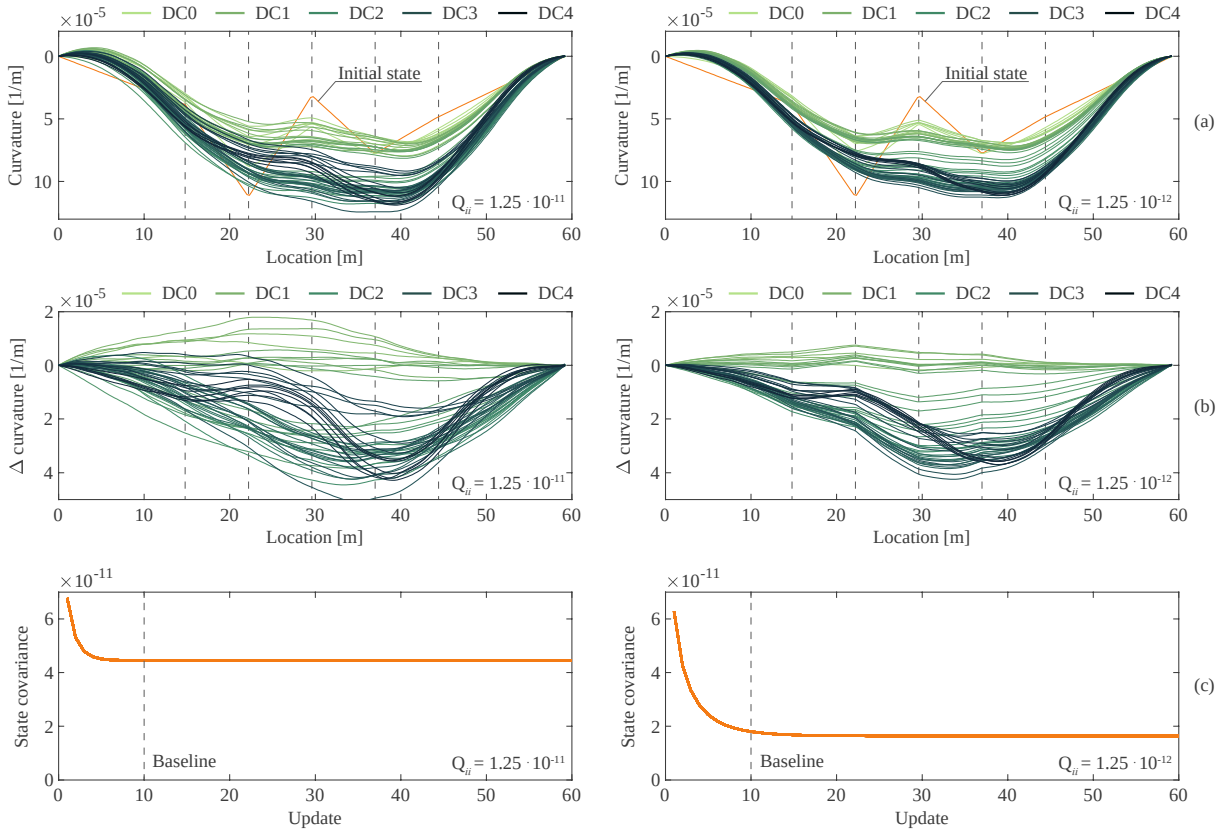

Figure 6 – Outcomes of the Kalman filter for different process noise: (a) updated state, (b) damage index, (c) state covariance

In order to better visualize the damage index, the results obtained at the last inspection of each damage configuration are reported in Figure 7a for $\mathbf{Q} = \mathbf{R}^{\mathrm{UL}}/100$. Besides, Figure 7b shows the curvature difference between consecutive damage scenarios using the same process noise.

In the results of this study, after inducing the first damage to the vertical element T1, a considerable curvature variation is visible for the entire structure, with a maximum at the midspan, which is the location of the damaged element. A following complete cut of the element (DC2) led to a further variation of the curvature profile, which is modest compared to the first. It should be noted that DC1 can be considered as a minor damage condition, as the element T1 is almost unloaded during ordinary loading conditions due to the almost coaxial elements of the top chord of the truss structure.

The retrofit intervention between DC2 and DC3 did not restore the original structural configuration, as the absolute magnitude of the curvature variation of DC3 is considerably lower than that of DC1 in Figure 7b. This curvature variation is almost triangular, with a peak at the location of the retrofitted element, reflecting the expected curvature variation.

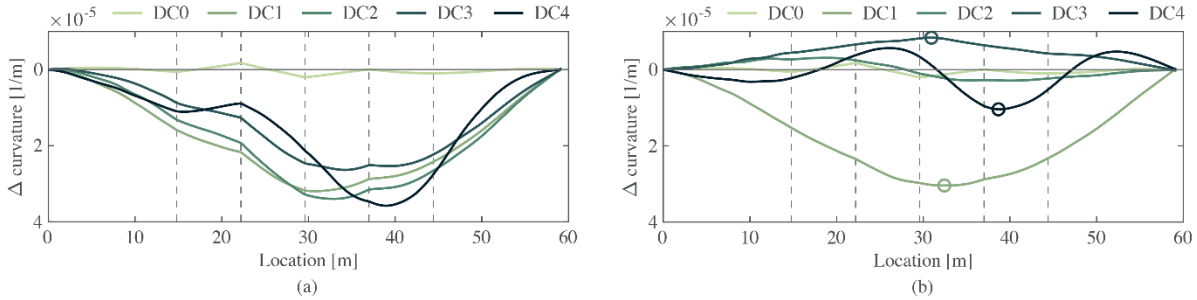

Figure 7 – Damage index at five inspection instants: (a) difference from the baseline, (b) difference from the previous configuration

Considering the last damage configuration, Figure 7a shows a global curvature variation similar to that of DC3, with an additional clear peak at the location of T2. This confirms an accurate localization of the structural anomalies. Since the structure in DC3 is still damaged due to the residual curvature difference with respect to the baseline DC0, condition DC4 represents the case of multiple damages, both in T1 and T2. Also, Figure 7b shows an oscillatory curvature variation profile between the retrofitted configuration and DC4. This can be explained considering that, in the case of a truss structure with traffic loads traveling on the deck, the reconstructed curvature profile is relevant to the bridge deck, which is retained by the nodes of the truss structure. Also, in contrast with the damage in T1, damage in T2 does not cause a considerable variation in the global structural behavior, mostly affecting the lower horizontal elements between sensors A3 and A5.

Figure 8 shows the results for the same five inspection instants obtained by updating the state of the system using a single type of measurement, i.e., (a) modal parameters or (b) influence lines. If the state is updated using only modal parameters, the curvature estimate is almost coincident in DC0 and DC1, thus resulting in a false negative when the vertical element T1 is partially damaged. Similar to the results found by Chang and Kim [44], DC2 has a considerably higher damage indicator. Kim et al. [47] observed a stress redistribution between DC0 and DC1, which may justify the slight variation of the damage indicator between the two configurations. Besides, using only modal parameters, damage in T2 is identified very well, as its location coincides with that of sensor A4.

On the other hand, in general, the influence line-based estimates are closer to the result obtained in Figure 7, yet, less sharp, especially in DC3, in which a clear peak is not identified in Figure 8.

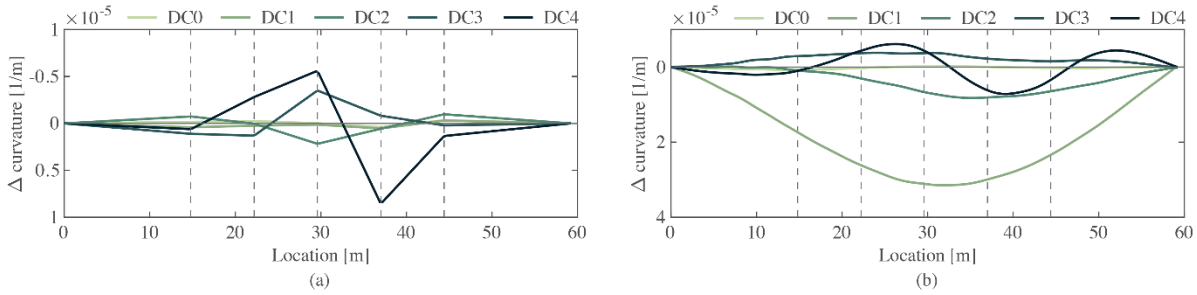

Figure 8 – Damage index at five inspection instants computed with respect to the previous configuration: (a) state updated using only modal parameters and (b) state updated using only quasi-static features

The main difference observed between the damage indicators obtained from modal parameters and influence lines is that, in the first case, DC1 variates slightly from the baseline, while DC2 has a considerable curvature increment. On the other hand, using influence lines, DC1 and DC2 both present an evident curvature variation from the baseline, while the variation is less pronounced between the two damaged configurations. This result may be justified considering the nonlinear behavior of the structure. If, after the first cut of T1, the structure experienced a residual deformation (with a plastic elongation of the element T1), modal parameters may not be substantially affected by this phenomenon, as the element T1 has a residual stiffness in DC1, which contributes to the dynamic equilibrium between elastic and distributed inertial forces. The damage becomes

evident in DC2, as noted by Chang and Kim [44], when the element T1 is completely cut and does not contribute to the structural stiffness. On the other hand, the influence lines are the double derivatives of the deflection of the bridge due to a concentrated traveling load. After the first cut of T1, the bridge may experience a higher displacement under traveling loads, which reflects in a higher identified curvature. Moreover, after the first reduction of the cross-sectional area of T1, the structure accumulated a residual inelastic deformation due to the structural and vehicle weight, as evident in Figure 4e. Starting from this relaxed configuration, it is possible that a complete cut of T1 generated a less apparent effect on the quasi-static structural response induced by concentrated traveling loads compared to that of the first partial cut.

4.2.2 Partial sensor setup

In general, all the results reported so far represent the real damage location accurately. However, the locations of damaged elements were coincident with some instrumented sections. A further study is carried out to identify high-resolution damage locations using only the two side sensors (i.e., A1 and A5), not deployed at the locations of damaged elements. Figure 9 reports the ULLs and dense curvature profiles obtained using modal parameters and quasi-static features, respectively, when only the data of the side sensors are employed.

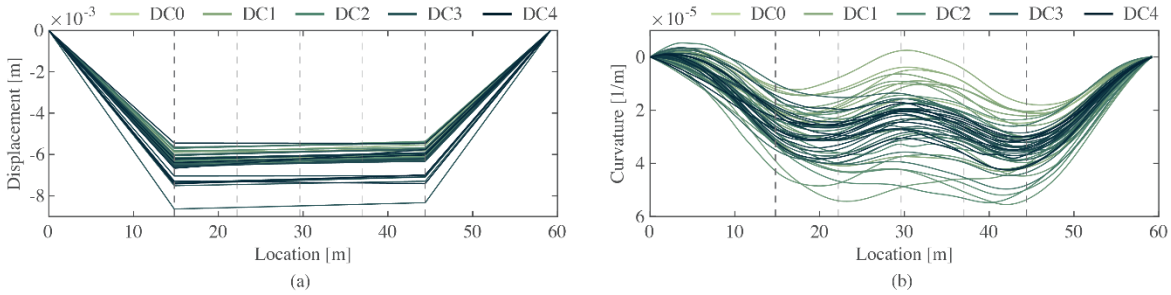

Figure 9 – Identified parameters using only the side sensors: (a) uniform load lines from modal parameters, (b) dense curvature profiles from quasi-static structural response

The KF is applied with the same parameters as described in the application with the full sensor setup, and a process noise matrix defined as $\mathbf{Q} = \mathbf{R}^{\mathrm{UL}}/100$. Figure 10 shows the state update and damage indicators calculated with respect to the baseline curvature profile obtained for all the 60 inspections (considering the first 10 samples as an initialization interval). Similar to the application shown in Section 4.2.1, the state estimates are considerably more stable than the individual curvature measurements in Figure 9, and their evolution over time is clear.

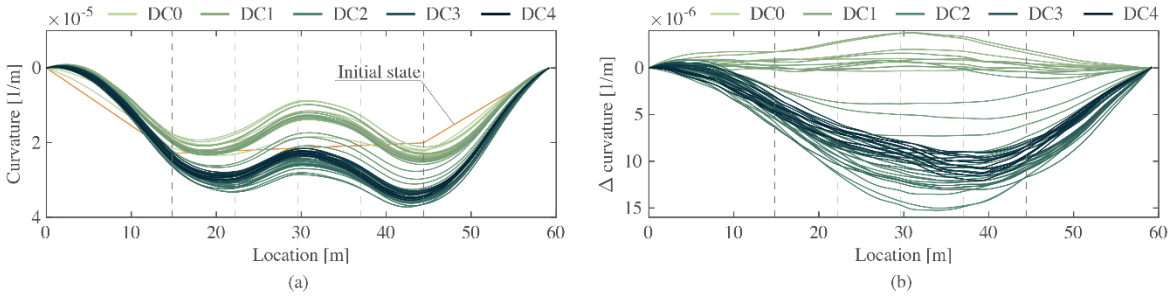

Figure 10 – Outcomes of the Kalman filter using only the side sensors: (a) updated state and (b) damage index

Figure 11 shows the damage indicator computed with respect to (a) the baseline and (b) the previous damage configuration, considering three inspection instants selected at the end of the intervals relevant to DC1, DC3, and DC4. It is worth noting that, although the sensors employed in this analysis were not deployed at the damage locations, the maxima of the damage indicators are close to T1 (in DC1 and DC3) and T2 (in DC4). Maximum values are highlighted using small circles in Figure 11b, which are almost in the same location as Figure 7. This result confirms that high-resolution damage localization can also be achieved by employing extremely sparse sensor networks.

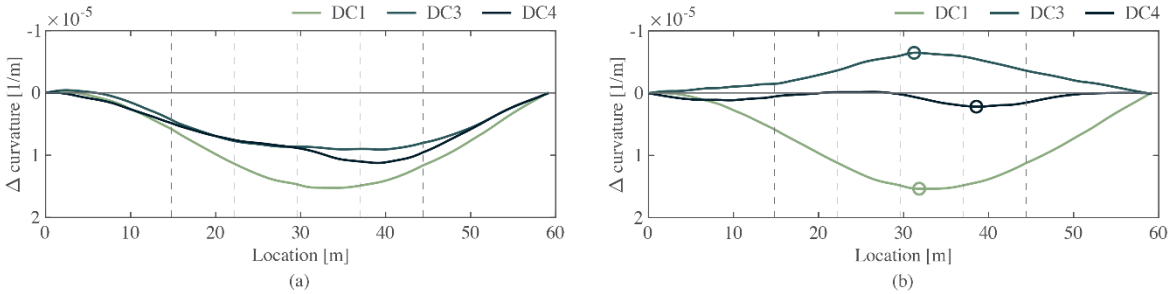

Figure 11 – Damage index at three inspection instants using only the side sensors: (a) difference from the baseline and (b) difference from the previous configuration

It is worth noting that, while the procedure proposed in this paper was formalized for uniform beams, the ADA bridge has a varying cross-section. Nevertheless, the results have shown that the method can still localize damage with high resolution. More details on the effects of a varying-cross section are reported in Section 4.4.

4.3 Effects of different lanes

This section reports the results obtained using the FE model of the ADA Bridge described in Section 4.1 for the simulated conditions DCs1, DCs2, and DCs3. In the simulations, 20 vehicle passages (10 for each direction, with a vehicle speed of 40 km/h and weight of 21 kN) were simulated for each damage condition and for an undamaged (reference) condition. The acceleration signals were corrupted by adding white Gaussian noise with a standard deviation equal to 1% of that of the original signal. This noise level is considered realistic, as the vibration amplitude induced by moving vehicles is relatively high.

The acceleration signals collected at locations A1 and A5 were processed using the same filter bank described in Section 4.2. The filtered signals were then employed to calculate ULL curvature and quasi-static features, fused using the same KF described in the previous section. The noise covariance matrix was set as a diagonal matrix with constant non-zero elements equal to the mean of the diagonal of the covariance matrix obtained from the 10 estimates of the dense curvature profile identified in the undamaged condition. In these analyses, $\mathbf{Q} = \mathbf{R}^{\mathrm{UL}}/10$.

The resulting states of the KF updated at each new inspection (i.e., vehicle passage) are reported in Figure 12. Here, all the inspections are represented as fine lines, while the last inspection for each damage condition is represented with a thicker line. Also, Figure 12(a) shows the curvature variations with respect to the baseline condition obtained for the vehicles traveling in Direction 1, while Figure 12(b) shows the same damage index obtained for the vehicles traveling in Direction 2. It is possible to notice that, for both directions, clear local maxima are identified at the locations of the damaged elements. In particular, the damage index in DCs1 shows a prominent peak close to element T3. The curvature variation in DCs2 is very similar to that in DCs1, although affecting a wider structural portion on the side of element T4 (this is especially visible in Figure 12(a)). Lastly, the curvature variation in DCs3 also presents an additional peak at the location of T5.

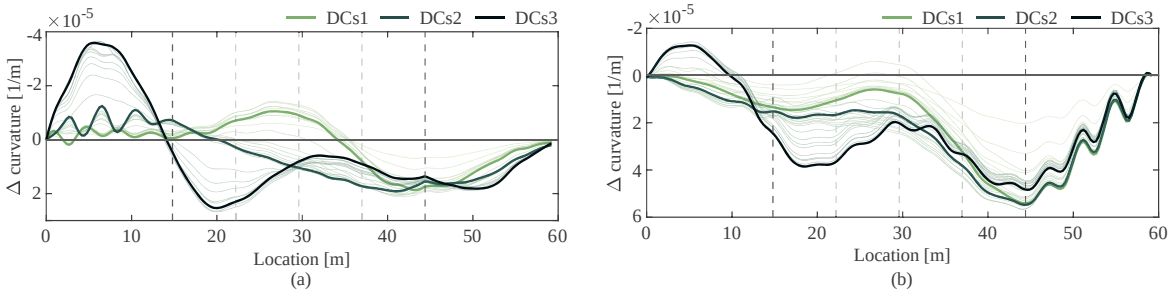

Figure 12 – Damage index for the simulated structure: (a) vehicle moving in Direction 1, (b) vehicle moving in Direction 2

It is worth noting that, in general, the damage index is higher when the vehicles travel in Direction 2, as they are closer to the instrumented locations. On the other hand, the side of the damaged element is not directly correlated with the amplitude of the damage index, as the different peaks identified in DCs3 (relevant to damaged elements on the two sides of the bridge deck) have a similar magnitude for both directions.

4.4 Effects of non-uniform cross-section

The procedure presented in Section 2 is specialized for simply supported structures with a uniform cross-section. However, the procedure can still be used for bridges with a non-uniform cross-section, accepting higher errors in the normalization process.

Five different beam configurations (C1, C2, C3, C4, and C5) were modeled with an overall length of 59.2 m and divided into 8 segments with the same length having a piecewise constant stiffness equal to $EI_{i,c} = 2 \cdot 10^7 \theta_i \; kN \cdot m^2$, where c denotes the beam configuration number (C1-C5), i is the segment index, and θ_i is a stiffness factor reported in Table 2 for each configuration and segment index.

Table 2 – Stiffness distribution factors

Element	1	2	3	4	5	6	7	8
C1	1	1	1	1	1	1	1	1
C2	0.85	0.9	0.95	1	1	0.95	0.9	0.85
C3	0.7	0.8	0.9	1	1	0.9	0.8	0.7
C4	0.4	0.6	0.8	1	1	0.8	0.6	0.4
C5	0.1	0.4	0.7	1	1	0.7	0.4	0.1

In order to quantify the uniformity of the cross-section along the beam, a uniformity parameter Θ is defined as follows:

$$\Theta_c = \frac{\left(\sum_{i=1}^{n} \theta_{i,c}\right)^2}{n \sum_{i=1}^{n} {\theta_{i,c}}^2} \tag{40}$$

with n denoting the total number of segments. Specifically, $\Theta_c = 1$ if the beam is uniform (i.e., in C1) and Θ_c decreases as the beam becomes more non-uniform.

Figure 13 shows the equivalent (EI_{eq}) and identified (EI_{id}) overall stiffness for the different configurations, together with the relative error between these two estimates. Specifically, the equivalent stiffness was calculated using the following equation, which represents the relation between the stiffness and displacement (d) at the midspan of a simply supported beam with uniform cross-section loaded at the midspan with a unitary load:

$$EJ_{eq} = \frac{l^3}{48d} \tag{41}$$

On the other hand, the identified stiffness was calculated using Equation (27).

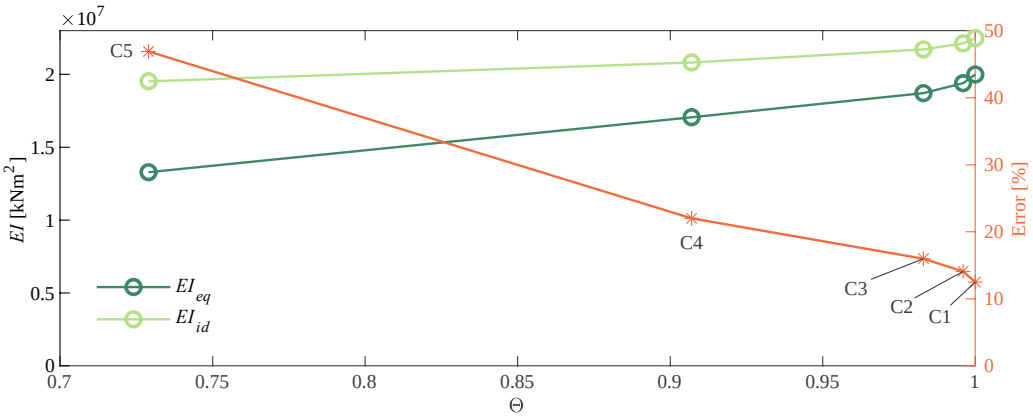

Figure 13 – Equivalent and identified overall stiffness for beams with non-uniform cross-section

The results show that, even in configuration C1, the error is non-zero (precisely, 12.5%) due to the approximations considered in the method. However, up to configuration C4, with a uniformity index equal to 0.907, the error is around 20% (precisely, 22.0%). On the other hand, a strongly non-uniform configuration (e.g., C5) may lead to errors of about 50% (in this case, 46.9%).

It should be noted that errors in the identified overall stiffness affect the feature normalization and, therefore, the relative contribution of modal parameters and quasi-static features in the determination of the damage index. While an exact quantification of the curvature variation may be difficult for bridges with strongly varying cross-sections, the localization ability of the algorithm is modestly affected, as evident from the results obtained in Section 4.2.

5. CONCLUSIONS

This paper presented an original method to identify dense and robust bridge features from sparse acceleration measurements collected during the passage of moving vehicles. Raw accelerations were decomposed into quasi-static and dynamic components, from which curvature influence lines and mode shapes were calculated. This process was carried out by filtering acceleration time histories through lowpass and bandpass filters, constituting a unique filter bank. Quasi-static and dynamic features were then employed to obtain two different estimates of the structural curvature, which were fused using a Kalman filter.

The state of the system, representing the dense curvature profile of the structure at the latest inspection time, has shown to be an effective damage-sensitive feature. Indeed, an indicator with a high spatial resolution for damage identification was obtained simply by subtracting the updated state of the system and a baseline estimate obtained at the beginning of the monitoring process or in a previous inspection time.

The method was applied to a real case study consisting of a steel truss bridge with artificially induced damage configurations and a simulated finite element model of the same bridge. Accurate results were obtained for different damage and retrofit configurations, both for dense sensor layouts involving devices deployed close to the damaged elements and for extremely sparse sensor layouts consisting of two uniaxial accelerometers deployed far from the damaged parts. The damage indicator presented the same maximum locations using the two sensor configurations, showing that effective damage localization is possible even with low-cost setups. However, more prominent peaks were obtained in the full sensor setup.

Besides, the effects of different load locations and structural configurations were investigated, showing that the method can be applied even for structures that do not fully respect the assumptions of the method, obtaining however higher errors.

In the Kalman filter, different choices of the process noise led to different evolution speeds of the state vector. However, considering that degradation phenomena are typically slow in civil infrastructure, low

process noise provided more robust estimates, which may limit the occurrence of false positives in the damage identification process. Moreover, different choices of the process noise determine different lengths of the optimal initial stabilization interval of the state vector, thus impacting the selection of the baseline configuration.

Compared to an updating process based only on dynamic parameters, quasi-static features improved the spatial resolution of the damage index considerably. On the other hand, considering only influence lines in the updating process can generate spurious oscillations in the damage indicator related to the uncertainties of these features identified from very short datasets.

ACKNOWLEDGEMENTS

The authors would like to gratefully acknowledge the availability of data recorded on the Old ADA Bridge, available at [43].

REFERENCES

[1] D. Zonta, B. Glisic, S. Adriaenssens, Value of information: Impact of monitoring on decision-making, Structural Control and Health Monitoring. 21 (2014) 1043–1056. https://doi.org/10.1002/stc.1631.

[2] T. Toksoy, A.E. Aktan, Bridge-condition assessment by modal flexibility, Experimental Mechanics. 34 (1994) 271–278. https://doi.org/10.1007/BF02319765.

[3] Z. Zhang, A.E. Aktan, Application of Modal Flexibility and Its Derivatives in Structural Identification, Research in Nondestructive Evaluation. 10 (1998) 43–61. https://doi.org/10.1007/pl00003899.

[4] C.R. Farrar, K. Worden, Structural Health Monitoring: A Machine Learning Perspective, John Wiley and Sons, Ltd, 2012. https://doi.org/10.1002/9781118443118.

[5] R. Brincker, C.E. Ventura, Introduction to Operational Modal Analysis, John Wiley and Sons, Ltd, 2015. https://doi.org/10.1002/9781118535141.

[6] J. Li, K.A. Mechitov, R.E. Kim, B.F. Spencer, Efficient time synchronization for structural health monitoring using wireless smart sensor networks, Structural Control and Health Monitoring. 23 (2016) 470–486. https://doi.org/10.1002/stc.1782.

[7] D. Wu, S.S. Law, Damage localization in plate structures from uniform load surface curvature, Journal of Sound and Vibration. 276 (2004) 227–244. https://doi.org/10.1016/j.jsv.2003.07.040.

[8] T. Pothisiri, K.D. Hjelmstad, Structural Damage Detection and Assessment from Modal Response, Journal of Engineering Mechanics. 129 (2003) 135–145. https://doi.org/10.1061/(ASCE)0733-9399(2003)129:2(135).

[9] L. Sun, Y. Li, W. Zhang, Experimental Study on Continuous Bridge-Deflection Estimation through Inclination and Strain, Journal of Bridge Engineering. 25 (2020) 04020020. https://doi.org/10.1061/(ASCE)BE.1943-5592.0001543.

[10] M.J. Whelan, M. V. Gangone, K.D. Janoyan, N.A. Hoult, C.R. Middleton, K. Soga, Wireless operational modal analysis of a multi-span prestressed concrete bridge for structural identification, Smart Structures and Systems. 6 (2010) 579–593. https://doi.org/10.12989/sss.2010.6.5_6.579.

[11] Y.B. Yang, J.P. Yang, State-of-the-Art Review on Modal Identification and Damage Detection of Bridges by Moving Test Vehicles, International Journal of Structural Stability and Dynamics. 18 (2018) 1850025. https://doi.org/10.1142/S0219455418500256.

[12] Q. Mei, M. Gül, M. Boay, Indirect health monitoring of bridges using Mel-frequency cepstral coefficients and principal component analysis, Mechanical Systems and Signal Processing. 119 (2019) 523–546. https://doi.org/10.1016/j.ymssp.2018.10.006.

[13] F. Cavadas, I.F.C. Smith, J. Figueiras, Damage detection using data-driven methods applied to moving-load responses, Mechanical Systems and Signal Processing. 39 (2013) 409–425. https://doi.org/10.1016/j.ymssp.2013.02.019.

[14] W.Y. He, W.X. Ren, S. Zhu, Damage detection of beam structures using quasi-static moving load induced displacement response, Engineering Structures. 145 (2017) 70–82. https://doi.org/10.1016/j.engstruct.2017.05.009.

[15] X. Zheng, D.H. Yang, T.H. Yi, H.N. Li, Bridge influence line identification from structural dynamic responses induced by a high-speed vehicle, Structural Control and Health Monitoring. 27 (2020). https://doi.org/10.1002/stc.2544.

[16] Z. Wu, N.E. Huang, Ensemble empirical mode decomposition: A noise-assisted data analysis method, Advances in Adaptive Data Analysis. 1 (2009) 1–41. https://doi.org/10.1142/S1793536909000047.

[17] S. Braun, M. Feldman, Decomposition of non-stationary signals into varying time scales: Some aspects of the EMD and HVD methods, Mechanical Systems and Signal Processing. 25 (2011) 2608–2630. https://doi.org/10.1016/j.ymssp.2011.04.005.

[18] Z.-W. Chen, Q.-L. Cai, S. Zhu, Damage quantification of beam structures using deflection influence lines, Structural Control and Health Monitoring. 25 (2018) e2242. https://doi.org/10.1002/stc.2242.

[19] H.H. Nassif, M. Gindy, J. Davis, Comparison of laser Doppler vibrometer with contact sensors for monitoring bridge deflection and vibration, NDT & E International. 38 (2005) 213–218. https://doi.org/10.1016/j.ndteint.2004.06.012.

[20] Z.-W. Chen, S. Zhu, Y.-L. Xu, Q. Li, Q.-L. Cai, Damage Detection in Long Suspension Bridges Using Stress Influence Lines, Journal of Bridge Engineering. 20 (2015) 05014013. https://doi.org/10.1061/(asce)be.1943-5592.0000681.

[21] G.T. Frøseth, A. Rønnquist, D. Cantero, O. Øiseth, Influence line extraction by deconvolution in the frequency domain, Computers and Structures. 189 (2017) 21–30. https://doi.org/10.1016/j.compstruc.2017.04.014.

[22] N.-B. Wang, L.-X. He, W.-X. Ren, T.-L. Huang, Extraction of influence line through a fitting method from bridge dynamic response induced by a passing vehicle, Engineering Structures. 151 (2017) 648–664. https://doi.org/10.1016/j.engstruct.2017.06.067.

[23] B. Wu, G. Wu, C. Yang, Y. He, Damage identification method for continuous girder bridges based on spatially-distributed long-gauge strain sensing under moving loads, Mechanical Systems and Signal Processing. 104 (2018) 415–435. https://doi.org/10.1016/j.ymssp.2017.10.040.

[24] M.M. Alamdari, K. Kildashti, B. Samali, H.V. Goudarzi, Damage diagnosis in bridge structures using rotation influence line: Validation on a cable-stayed bridge, Engineering Structures. 185 (2019) 1–14. https://doi.org/10.1016/j.engstruct.2019.01.124.

[25] F. Huseynov, C. Kim, E.J. OBrien, J.M.W. Brownjohn, D. Hester, K.. Chang, Bridge damage detection using rotation measurements – Experimental validation, Mechanical Systems and Signal Processing. 135 (2020) 106380. https://doi.org/10.1016/j.ymssp.2019.106380.

[26] R. Zaurin, T. Khuc, F.N. Catbas, Hybrid Sensor-Camera Monitoring for Damage Detection: Case Study of a Real Bridge, Journal of Bridge Engineering. 21 (2016) 05016002. https://doi.org/10.1061/(ASCE)BE.1943-5592.0000811.

[27] A. Martini, E.M. Tronci, M.Q. Feng, R.Y. Leung, A computer vision-based method for bridge model updating using displacement influence lines, Engineering Structures. 259 (2022) 114129. https://doi.org/10.1016/j.engstruct.2022.114129.

[28] S. Quqa, L. Landi, P.P. Diotallevi, Automatic identification of dense damage-sensitive features in civil infrastructure using sparse sensor networks, Automation in Construction. 128 (2021) 103740. https://doi.org/10.1016/j.autcon.2021.103740.

[29] S. Quqa, L. Landi, P. Paolo Diotallevi, P.P. Diotallevi, Instantaneous modal identification under varying structural characteristics: A decentralized algorithm, Mechanical Systems and Signal Processing. 142 (2020) 106750. https://doi.org/10.1016/j.ymssp.2020.106750.

[30] S. Quqa, A. Antolini, E. Franchi Scarselli, A. Gnudi, A. Lico, M. Carissimi, M. Pasotti, R. Canegallo, L. Landi, P.P. Diotallevi, Phase change memories in smart sensing solutions for structural health monitoring, Journal of Computing in Civil Engineering. 36 (2022) 04022013. https://doi.org/10.1061/(ASCE)CP.1943-5487.0001027.

[31] P.F. Giordano, M.P. Limongelli, Response-based time-invariant methods for damage localization on a concrete bridge, Structural Concrete. 21 (2020) 1254–1271. https://doi.org/10.1002/suco.202000013.

[32] L. Frýba, Vibration of Solids and Structures under Moving Loads, Springer Science & Business Media, 1999. https://doi.org/10.1680/vosasuml.35393.

[33] I. Talebinejad, H. Sedarat, A. Emami-Naeini, A. Krimotat, J. Lynch, Implementation of damage detection algorithms for the Alfred Zampa Memorial Suspension Bridge, in: H.F. Wu, T.-Y. Yu, A.L. Gyekenyesi, P.J. Shull (Eds.), 2014: p. 906312. https://doi.org/10.1117/12.2044539.

[34] G. Wolberg, Cubic Spline Interpolation: A Review, New York, NY, 1988. https://doi.org/10.7916/D82Z1DMQ.

[35] A. Sadhu, S. Narasimhan, J. Antoni, A review of output-only structural mode identification literature employing blind source separation methods, Mechanical Systems and Signal Processing. 94 (2017) 415–431. https://doi.org/10.1016/j.ymssp.2017.03.001.

[36] C.A. Perez-Ramirez, J.P. Amezquita-Sanchez, H. Adeli, M. Valtierra-Rodriguez, R. de J. Romero-Troncoso, A. Dominguez-Gonzalez, R.A. Osornio-Rios, Time-frequency techniques for modal parameters identification of civil structures from acquired dynamic signals, Journal of Vibroengineering. 18 (2016) 3164–3185. https://doi.org/10.21595/jve.2016.17220.

[37] S. Quqa, L. Landi, P. Paolo Diotallevi, Modal assurance distribution of multivariate signals for modal identification of time-varying dynamic systems, Mechanical Systems and Signal Processing. 148 (2021) 107136.

https://doi.org/10.1016/j.ymssp.2020.107136.
[38] N.E. Huang, Z. Shen, S.R. Long, M.C. Wu, H.H. Snin, Q. Zheng, N.C. Yen, C.C. Tung, H.H. Liu, The empirical mode decomposition and the Hubert spectrum for nonlinear and non-stationary time series analysis, Proceedings of the Royal Society A: Mathematical, Physical and Engineering Sciences. 454 (1998) 903–995. https://doi.org/10.1098/rspa.1998.0193.
[39] R.T. Rato, M.D. Ortigueira, A.G. Batista, On the HHT, its problems, and some solutions, Mechanical Systems and Signal Processing. 22 (2008) 1374–1394. https://doi.org/10.1016/j.ymssp.2007.11.028.
[40] M. Vetterli, J. Kovačević, Wavelets and Subband Coding, Prentice-hall, 1995.
[41] M.A. Pisani, M.P. Limongelli, P.F. Giordano, M. Palermo, On the Effectiveness of Vibration-Based Monitoring for Integrity Management of Prestressed Structures, Infrastructures. 6 (2021) 171. https://doi.org/10.3390/infrastructures6120171.
[42] C.-W. Kim, F.-L. Zhang, K.-C. Chang, P.J. McGetrick, Y. Goi, Ambient and Vehicle-Induced Vibration Data of a Steel Truss Bridge Subject to Artificial Damage, Journal of Bridge Engineering. 26 (2021) (ASCE)BE.1943-5592.0001730. https://doi.org/10.1061/(ASCE)BE.1943-5592.0001730.
[43] C.-W. Kim, F. Zhang, K.-C. Chang, P. McGetrick, Y. Goi, Old_ADA_Bridge-damage_vibration_data, (2021). https://doi.org/10.17632/sc8whx4pvm.2.
[44] K.-C. Chang, C.-W. Kim, Modal-parameter identification and vibration-based damage detection of a damaged steel truss bridge, Engineering Structures. 122 (2016) 156–173. https://doi.org/10.1016/j.engstruct.2016.04.057.
[45] I. Daubechies, Ten Lectures on Wavelets, 1992. https://doi.org/10.1137/1.9781611970104.
[46] M. Nielsen, On the Construction and Frequency Localization of Finite Orthogonal Quadrature Filters, Journal of Approximation Theory. 108 (2001) 36–52. https://doi.org/10.1006/jath.2000.3514.
[47] C. Kim, K. Chang, S. Kitauchi, P. McGetrick, K. Hashimoto, K. Sugiura, Changes in modal parameters of a steel truss bridge due to artificial damage, in: Safety, Reliability, Risk and Life-Cycle Performance of Structures and Infrastructures, CRC Press, 2014: pp. 3725–3732. https://doi.org/10.1201/b16387-541.